INL/EXT-14-33251

Light Water Reactor Sustainability Program

Grizzly Status Report

September 2014

DOE Office of Nuclear Energy

INL/EXT-14-33251

Light Water Reactor Sustainability Program

Grizzly Status Report

Benjamin Spencer[1], Yongfeng Zhang[1], Pritam Chakraborty[1], Marie Backman[2], William Hoffman[1], Daniel Schwen[1], S. Bulent Biner[1], Xianming Bai[1]

[1]Idaho National Laboratory
[2]University of Tennessee

September 2014

Idaho National Laboratory
Idaho Falls, Idaho 83415

http://www.inl.gov/lwrs

Prepared for the
U.S. Department of Energy
Office of Nuclear Energy
Under DOE Idaho Operations Office
Contract DE-AC07-05ID14517

EXECUTIVE SUMMARY

This report summarizes work during FY 2014 to develop capabilities to predict embrittlement of reactor pressure vessel steel, and to assess the response of embrittled reactor pressure vessels to postulated accident conditions. This is an inherently multiscale problem. Material embrittlement occurs due to phenomena occurring at the atomistic scale. The effects of these lower length scale phenomena must be accounted for in models up to the engineering scale. As such, the efforts underway in Grizzly span these scales, as described below.

At the engineering scale, 3D fracture mechanics capabilities have been developed to calculate stress intensities and fracture toughnesses, to perform a deterministic assessment of whether a crack would propagate at the location of an existing flaw. This capability has been demonstrated on several types of flaws in a generic reactor pressure vessel model.

Models have been developed at the scale of fracture specimens to develop a capability to determine how irradiation affects the fracture toughness of material. Verification work has been performed on a previously-developed model to determine the sensitivity of the model to specimen geometry and size effects. The effects of irradiation on the parameters of this model has been investigated.

At lower length scales, work has continued in an ongoing to understand how irradiation and thermal aging affect the microstructure and mechanical properties of reactor pressure vessel steel. Previously-developed Atomic Kinetic Monte Carlo models have been further developed and benchmarked against experimental data. Initial work has been performed to develop models of nucleation in a phase field model. Additional modeling work has also been performed to improve the fundamental understanding of the formation mechanisms and stability of matrix defects caused.

CONTENTS

FIGURES

TABLES

ACRONYMS

AKMC	Atomic Kinetic Monte Carlo
ASTM	American Society of Testing and Materials
BCC	Body centered cubic
CRP	Cu Rich Precipitate
CZM	Cohesive zone model
DBT	Ductile to Brittle Transition
DBTT	Ductile to Brittle Transition Temperature
DFT	Density Functional Theory
DPA	Displacements per Atom
DXA	Dislocation extraction algorithm
EONY	Eason, Odette, Nanstad, and Yamamoto
EPRI	Electric Power Research Institute
FE	Finite Element
GTN	Gurson Tvergaard Needleman
KMC	Kinetic Monte Carlo
LWR	Light water reactor
MMC	Metropolis Monte Carlo
MNP	Mn/Ni Rich Precipitate
PTS	Pressurized Thermal Shock
PCCv	Pre-cracked Charpy V-notch
RPV	Reactor Pressure Vessel
SENB	Single edge notched beam
SIA	Self Interstitial Atom

TEM	Tunneling Electron Microscope
TE	Total elongation
UE	Uniform elongation
UTS	Ultimate tensile strength
VVF	Void volume fraction
YS	Yield strength

1 Introduction

1.1 Materials aging and degradation in light water reactors

Materials used in nuclear reactors are subject to complex degradation processes due to the long service time in harsh environments that combine the effects of conditions such as high temperature, stress, neutron irradiation and corrosive media [2]. Extension of the reactor lifetime exerts further challenges to these materials. The safe operation of reactors requires methods and tools for a reliable assessment of the material performance during the service time.

Depending on the chemical components, fabrication histories and operation conditions, reactor materials may experience very different degradation processes [3]. Detailed documentation of the materials in light water reactors (LWRs) and corresponding degradation mechanisms of potential concern can be found in the Progressive Materials Degradation Approach (PMDA) report NUREG/CR-6923 by US Nuclear Regulatory Commission (NRC) [4] and the Materials Degradation Matrix (MDM) by the Electric Power Research Institute (EPRI) [5].

Several key material performance issues identified in these studies that can potentially limit the serviceable lifetime of a nuclear power plant include the embrittlement of reactor-pressure-vessel (RPV) steels, irradiation-assisted-stress-corrosion-cracking (IASCC) of reactor core internals, aging and fatigue of primary systems, corrosion of primary piping and secondary systems and aging of concrete containment. In these cases, the degradation may be caused by one or more environmental factors such as temperature, stress, irradiation and corrosive media. The variety in chemical composition and microstructure of these materials due to the fabrication process further increases the complexity in the degradation mechanisms.

Major nuclear power plant reactor components are usually very expensive to repair or replace. Hence, the ability to perform a predictive assessment of the material performance during extended service is critical to ensure the safe operation of plants during lifetime extensions, and for the process of making decisions regarding lifetime extensions. Such assessments require fundamental understanding of the degradation mechanisms, as well as analysis tools that can predict these degradation mechanisms and the ability of the components to safely perform their functions after being subjected to degradation.

1.2 Grizzly scope

The Grizzly software [6] is being developed under the LWRS program to provide a tool for predictive assessment of aging and material degradation mechanisms that may limit the lifetime of current LWRs. It is developed under the INL's MOOSE multiphysics simulation environment [7]. The goal is to incorporate as much as possible fundamental understanding of degradation mechanisms at the microstructure level. Initial development of Grizzly began in FY 2012, and the initial focus has been on the mechanisms causing embrittlement in reactor pressure vessel steel, and on predicting the capacity of embrittled vessels. Future work is planned to address aging issues in a variety of other components, including containment vessels, core internal structures, piping, and cables. An initial literature survey on concrete aging mechanisms was completed in FY 2014 [8], and plans are underway to begin developing models for aging processes in concrete.

RPVs in LWRs are usually made of low-alloy steels with the bainitic (primarily ferrite with cementite) microstructure [9]. In RPV steels, the main alloying elements are Mn, Ni, C and Si, with Cu being either an alloying element or an impurity. During service, RPVs are subject to both high temperature (about 300°C) and radiation damage induced by fast neutrons. As a result, Cu-rich precipitates (CRPs) may form since Cu is almost insoluble in bcc Fe. Another type of precipitates rich of Ni and Mn, i.e., the so-call late-blooming phase [10], may also form at high irradiation dose. Meanwhile, neutron irradiation produces lattice defects such as vacancies and self-interstitial-atoms (SIAs), and their agglomerates including voids and defect loops.

Both the precipitates and lattice defects impede dislocation motion, resulting in hardening and consequent embrittlement of RPV steels.

An engineering scale evaluation of RPV embrittlement needs information on the microstructure, which evolves as solute precipitation and defect accumulation occurs concurrently. It also needs accurate evaluation on the reduction of fracture toughness due to the change in microstructure. Empirical or semi-empirical approaches have been utilized to assess RPV embrittlement within the lifetime of current reactors. However, the lack of mechanistic understanding and experimental data strongly limits the extrapolation of these models beyond 60 years to assist decision-making on possible lifetime extension. A major goal of the Grizzly application is to provide validated engineering models based on fundamental understanding of microstructure evolution that can predict the capacity of RPVs subjected to a service life beyond 60 years.

1.3 Previous efforts and FY 2014 tasks

In the first year (FY 2012) of the Grizzly effort, an initial proof of concept was performed to demonstrate Grizzly's ability to predict global RPV thermo-mechanical response under pressurized thermal shock (PTS) loading conditions [11]. In addition, the degradation of material properties was evaluated using the EONY model [12] in this demonstration, although at that time, there were no fracture capabilities available in Grizzly to use these properties in an engineering assessment.

In FY 2013, further development of Grizzly proceeded toward the goal of developing a capability for engineering scale fracture assessment of capability of embrittled RPVs. In addition, work was begun to develop methods to characterize material microstructure evolution and the consequent reduction in fracture toughness [6]. Specifically, at the engineering scale, a global thermo-mechanical model of a RPV subjected to pressurized thermal shock loading conditions was benchmarked against solutions of the FAVOR code [13]. A capability to drive the boundary conditions for detailed submodels of the region surrounding a fracture was also developed. Progress was also made toward developing a general fracture J-integral integration capability. At the fracture specimen scale, a unified cohesive zone model was developed to predict the brittle to ductile transition and demonstrated to show good agreement with experimental results for fracture toughness and stable crack growth. At the atomic scale, an Atomic Kinetic Monte Carlo (AKMC) model [14] and a Metropolis Monte Carlo (MMC) algorithm were developed to investigate solute precipitation, with the material properties obtained through molecular dynamics (MD) simulations. The atomic scale information on microstructure will inform the fracture test scale fracture mechanics model development, which will ultimately be used in the engineering scale for RPV performance under various loading scenarios.

In FY 2014, additional development work has continued across these same length scales. At the engineering scale, the fracture mechanics capabilities have been extended to permit the evaluation of J-integrals to obtain stress intensities for axis-aligned flaws in RPVs. The full set of capabilities needed to perform an engineering assessment of crack propagation at an existing axis-aligned flaw is now in place, so the loading can be compared to the capacity as calculated using the EONY model. At the fracture specimen scale, efforts have continued to validate the unified cohesive zone model previously developed to predict ductile to brittle transition behavior in RPV steels. The effects of specimen geometry and size on this model have been investigated, as have the effects of irradiation on the input parameters for this model. At the lower-length-scale (atomic to meso), further development of the AKMC model has been done to relate the KMC time to actual time, and to benchmark the AKMC results with thermal aging experiments. MD simulations have also been performed to explore the structural evolution of radiation induced lattice defects in bcc Fe to improve fundamental understanding in this area. Development of phase field models for precipitate nucleation and growth at larger length and time scale has also begun. Starting with the engineering scale, and then working through the specimen scale and lower length scales, the progress in this project during the current year is summarized in this report. At the end of each of these sections, summaries and plans for future work are provided.

2 Engineering scale

2.1 Demonstration of 3D analysis of flaws in a RPV

In a pressurized thermal shock (PTS) loading event in a RPV, there is concern that the low temperature would decrease the fracture toughness sufficiently that the loading-induced stress concentrations at pre-existing flaws in the wall could result in crack growth and propagation and potentially lead to a breach in the RPV wall. This risk is greater in older RPVs, where radiation embrittlement of the steel in the beltline region causes a significant decrease in the fracture toughness over the years that the reactor is in operation. The stress concentrations at crack tips can be evaluated in finite element simulations using detailed models of the geometry of the cracks if the stress and temperature profiles through the wall can be modeled. During the current fiscal year, Grizzly has been extended to enable it to evaluate domain integrals at crack tips in 3D in the presence of thermal loading. This allows for detailed deterministic analysis of the stress intensity factors along crack tips. This provides a way to assess the risk of crack growth at an existing flaw. Details about the implementation and testing of the 3D J-integral capability can be found in a separate report [15].

To model loading in the RPV wall, a full-scale 3D model was developed of a four-loop RPV with a 4 mm stainless steel liner on the inner surface. The model, shown in Fig. 1, has 660,000 elements and 10 elements through the thickness of the wall in the beltline region. The innermost element represents the stainless steel liner and has different material properties from the base metal, for instance, a higher thermal expansion coefficient. Two different PTS scenarios were modeled here. The coolant pressure and temperature histories were prescribed as boundary conditions at the inner surface of the RPV model. Temperature is prescribed using a time-varying heat transfer coefficient. The solutions for displacement and temperature in the global RPV model were used to drive several submodels containing a variety of axis-aligned flaws. The MOOSE framework provides functions for reading in a solution and interpolating it onto a different mesh and this capability was used to prescribe the global model solution as boundary conditions of submodels.

Four different submodel meshes were generated; two of semi-circular surface-breaking flaws with crack plane normal in the axial and circumferential direction, respectively, and of two circular embedded flaws, one of each orientation (Fig. 2). The flaws are penny shaped with a diameter of 2 cm and have blunt crack tips. The submodels were placed in the center of the beltline region as illustrated by the dark blue cube in Fig. 1 and share a symmetry plane with the global model at $y = 0$. The symmetry plane has boundary conditions forcing no displacement in the y-direction, and this surface and the other surfaces have prescribed displacements in the x, y, and z directions using values interpolated in space and time from the solution of the global RPV model. The surface-breaking flaws have displacements prescribed on five surfaces and on the surface facing the inner surface of the RPV the same pressure history as in the global model was prescribed. The temperatures are interpolated from the global model and prescribed at all nodes in the submodels.

Temperatures and pressures during two representative PTS transients are shown in Fig. 3. These are referred to here as a temperature-driven and a pressure-driven transient. The temperature-driven transient has a rapid drop in coolant temperature and pressure, and causes high tensile stresses in the interior of the RPV primarily due to the rapid temperature drop. The pressure-driven transient, on the other hand, is characterized by reduction of temperature and pressure at a lower rate, but includes a rapid re-pressurization, which can cause significant tensile stresses through the full vessel cross-section primarily due to the pressure load.

Using Grizzly's J-integral capability, the stress intensity factor K_I along the crack front was analyzed during the PTS transient. The applied K_I was compared to the fracture toughness K_{Ic} of the embrittled steel after 32 years of operation. On the right hand side of Fig. 1, the distribution of accumulated neutron fluence at this point in time is illustrated. The EONY model [16] provides an estimate of the ductile-to-brittle transition temperature shift of the pressure vessel steel at the prescribed neutron fluence. By using the calculated transition temperature in the fracture toughness master curve [17, 18], the critical stress intensity factor K_{Ic} can then be evaluated. The time history of K_I versus K_{Ic} is plotted in Fig. 4 for the pressure-driven

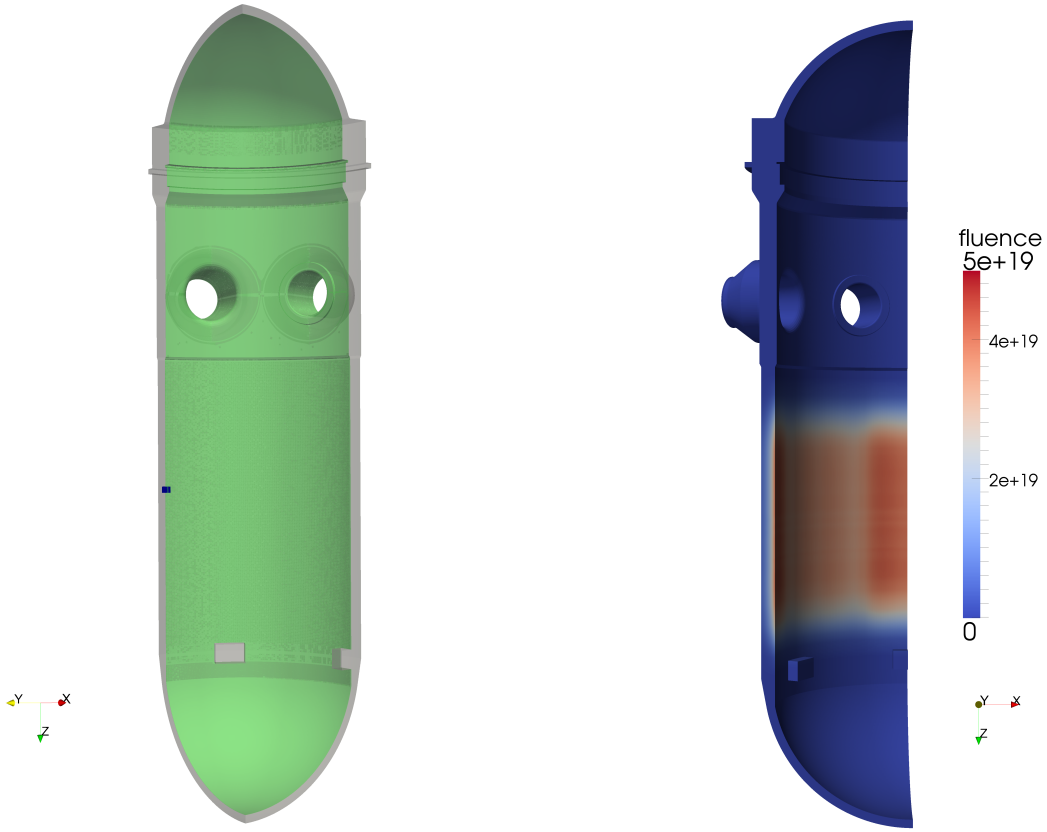

Figure 1: Global model of RPV showing location of submodel with detailed flaw geometry (blue region on left side) (left). The base material is colored gray, and the liner material is colored green. Distribution of accumulated neutron fluence after 32 years of operation (right).

transient and in Fig. 5 for the temperature-driven transient.

As a general conclusion, the temperature-driven transient (Fig. 4) is found to pose a more severe threat than the pressure-driven loading, as seen by the higher K_I values at the flaws and the relatively low fracture toughness K_{Ic} due to the low temperature of the coolant. One of the embedded flaws (Fig. 4c) has a K_I that exceeds the 1% probability of fracture over an extended period of time. In contrast, all the flaws loaded by the pressure-driven transient have a maximum stress intensity factor less than half the value of the 1% K_{Ic} and for most of the duration of the transient, it is significantly lower. The temperature during this transient stays on average much higher than for the temperature-driven one, which directly leads to the higher K_{Ic} and the comparatively low risk of fracture propagation.

2.2 Interaction integral implementation

PTS transients can induce complex loading conditions in a RPV and at pre-existing flaws in the wall. In structural integrity assessments of RPVs, flaws are often assumed to be under pure mode I loading to simplify analysis of stress intensity factors and their comparison with the known fracture toughness of the material. This is a valid assumption for axis-aligned flaws in the absence of residual stresses or other local effects that cause a departure from axisymmetric conditions. Because of a variety of effects such as flaw alignment, residual stresses, and variations in the coolant temperature, the loading on an actual flaw in a RPV is not necessarily pure mode-I, but can be a combination of modes I, II, and III.

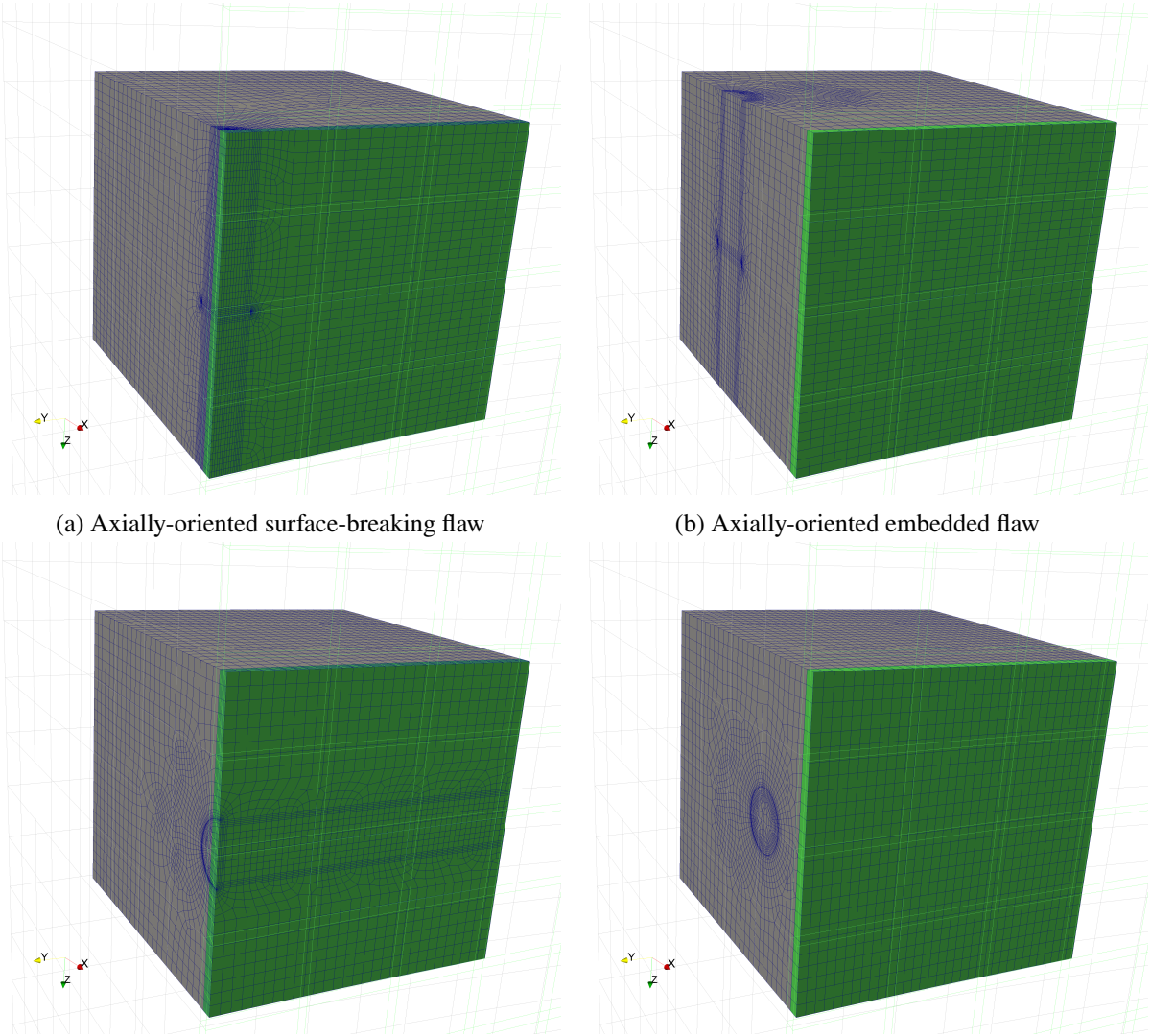

(a) Axially-oriented surface-breaking flaw

(b) Axially-oriented embedded flaw

(c) Circumferentially-oriented surface-breaking flaw

(d) Circumferentially-oriented embedded flaw

Figure 2: Submodels of various flaw geometries modeled in current study. The mesh of the global model is shown as a wireframe overlaid on each submodel mesh. The base material is colored gray, and the liner material is colored green.

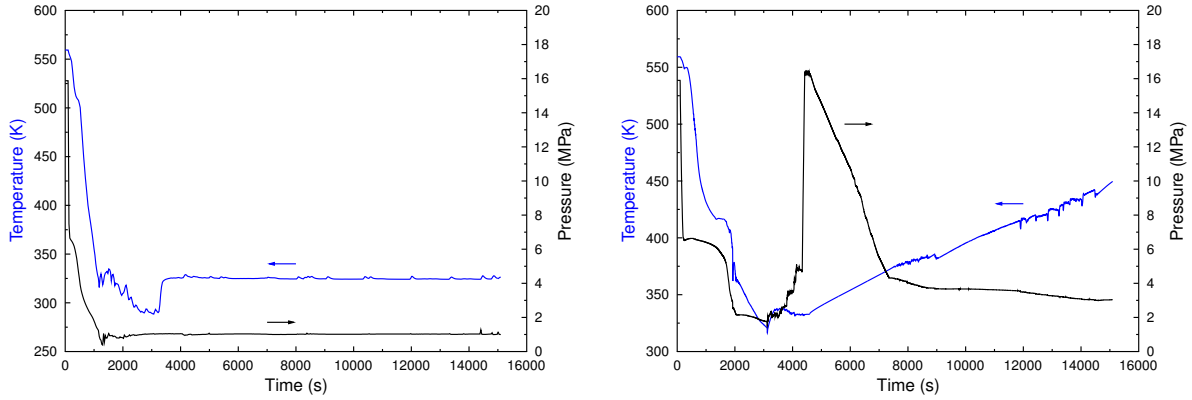

Figure 3: Temperature and pressure histories in a RPV for a temperature-driven transient (left) and a pressure-driven transient (right), applied as boundary conditions at the inner surface of the full scale RPV model.

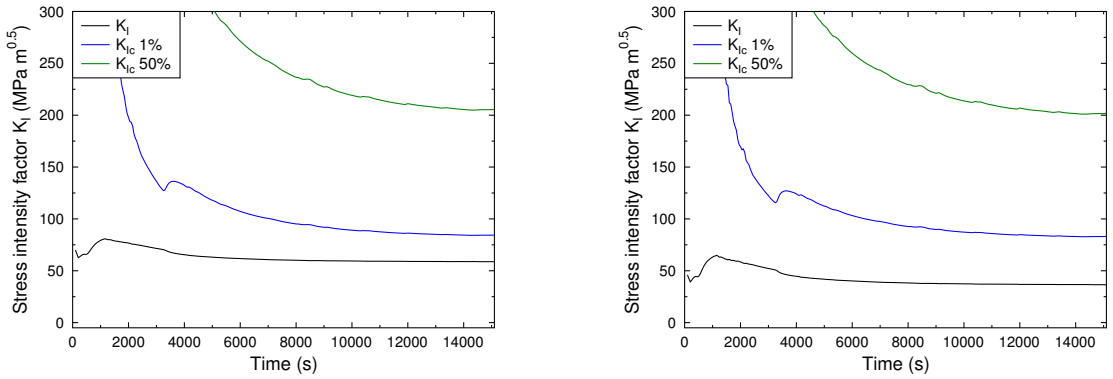

(a) Embedded flaw with crack plane normal in the circumferential direction

(b) Surface-breaking flaw with normal in the circumferential direction

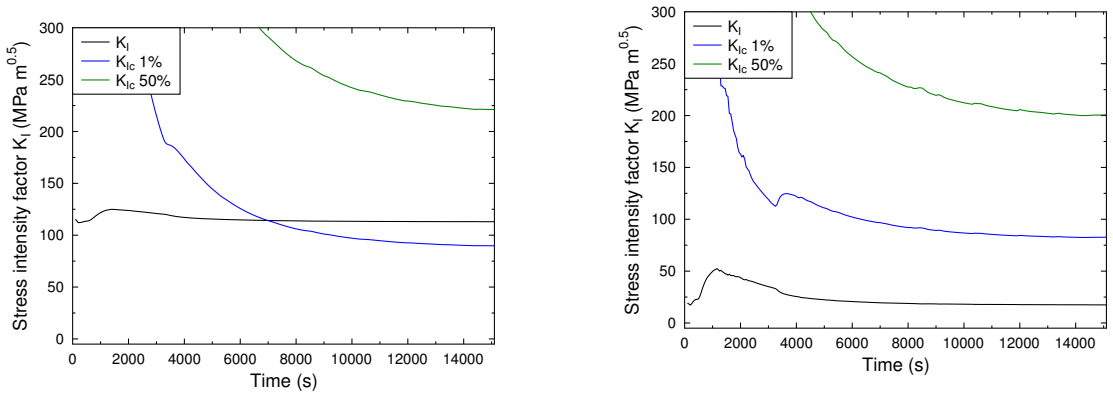

(c) Embedded flaw with normal in the axial direction

(d) Surface-breaking flaw with normal in the axial direction

Figure 4: Stress intensity factor K_I at the crack front compared to the critical stress intensity factor K_{Ic} with a failure probability of either 1% or 50% for the temperature-driven transient. It is worth noting that K_I for the embedded axial flaw 5c exceeds the 1% failure probability value of the fracture toughness K_{Ic}.

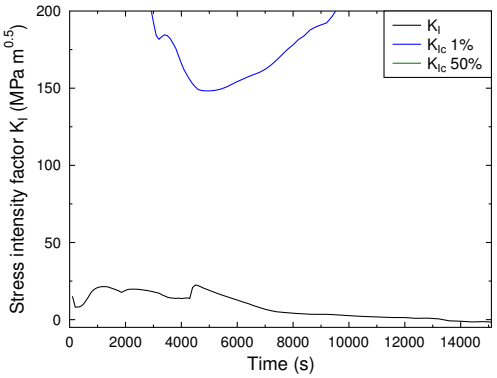

(a) Embedded flaw with crack plane normal in the circumferential direction

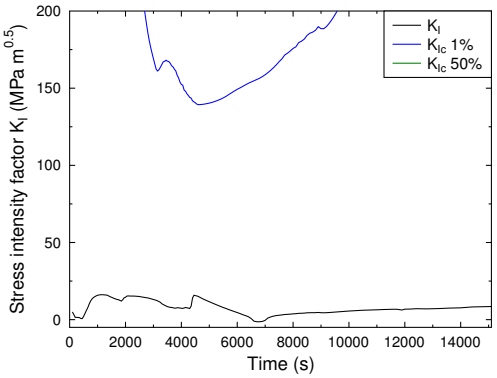

(b) Surface-breaking flaw with normal in the circumferential direction

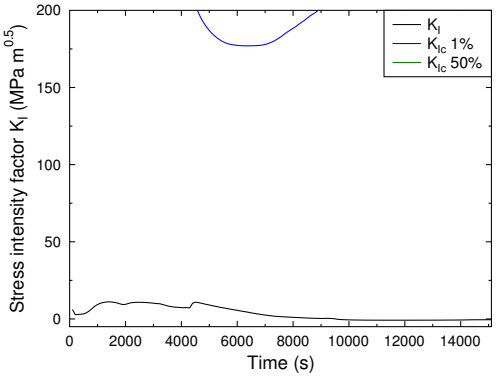

(c) Embedded flaw with normal in the axial direction

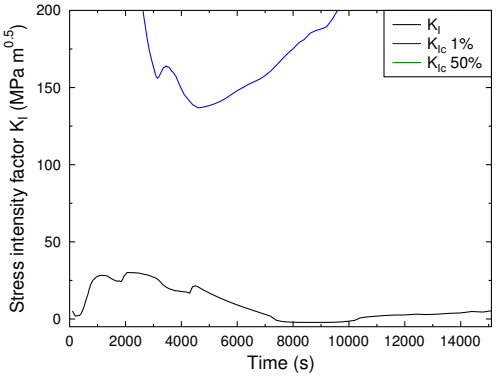

(d) Surface-breaking flaw with normal in the axial direction

Figure 5: Stress intensity factor K_I at the crack front compared to the critical stress intensity factor K_{Ic} with a failure probability of either 1% or 50% for the pressure-driven transient.

In the work presented thus far, the mode-I stress intensity is calculated from the J-integral. This is valid for pure mode-I loading, but not for general mixed-mode loading. The interaction integral method is based on the J-integral and makes it possible to evaluate mixed-mode stress intensity factors K_I, K_{II} and K_{III}, as well as the T-stress, in the vicinity of three dimensional cracks. The formulation relies on superimposing William's solution for stress and displacement around a crack (in this context called 'auxiliary fields') and the computed finite element stress and displacement fields (called 'actual fields'). The total superimposed J can be separated into three parts: the J of the actual fields, the J of the auxiliary fields, and an interaction part containing the terms with both actual and auxiliary field quantities. The last part is called the interaction integral and for a straight crack without thermal loading or crack face tractions, the interaction integral can be written as [19]:

$$I^S(s) = \int_V \left[\sigma_{ij} u^{\text{aux}}_{j,1} + \sigma^{\text{aux}}_{ij} u_{j,1} - \sigma_{jk} \epsilon^{\text{aux}}_{jk} \delta_{1i}\right] q_{,i} \, \mathrm{d}V \tag{1}$$

where σ is the stress, u is the displacement, and q is a weight function that represents the field of virtual displacements due to the virtual crack extension (identical to the q-functions used for J-integrals). By writing J in terms of the mixed-mode stress intensity factors, the interaction integral evaluates to:

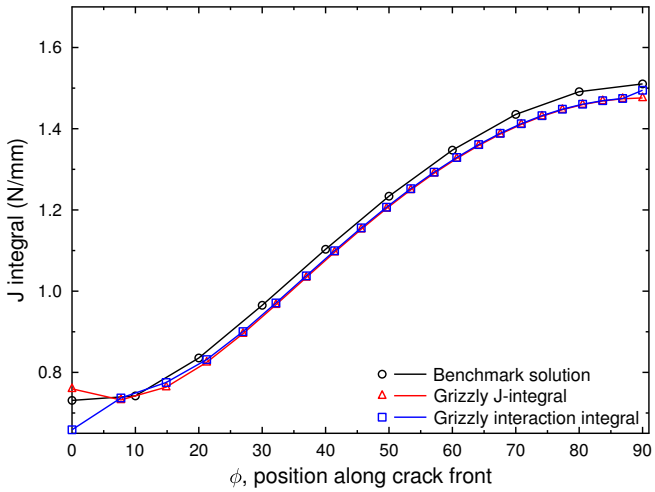

Figure 6: J-integral along the crack front of a semi-elliptic surface breaking crack loaded in Mode I under tension.

$$I^S(s) = \frac{1-\nu^2}{E}\left(2K_I K_I^{\text{aux}} + 2K_{II}K_{II}^{\text{aux}}\right) + \frac{1+\nu}{E}\left(K_{III}K_{III}^{\text{aux}}\right) \tag{2}$$

To obtain individual stress intensity factors, the interaction integral is evaluated with different auxiliary fields. For instance, by choosing $K_I^{\text{aux}} = 1.0$ and $K_{II}^{\text{aux}} = K_{III}^{\text{aux}} = 0$ and computing $I(s)$ in Eq. 1, K_I can be solved for in Eq. 2.

To enable the future assessment of flaws of arbitrary orientation, the interaction integral , as written in Eq. 1 and 2, has been implemented in Grizzly this year by building on its existing J-integral evaluation capability. The capability to evaluate the mode-I, II, and III stress intensities has been implemented, but to date, only the mode I stress intensity factor K_I has been tested. The mode-I interaction integral method was tested for a semi-elliptic surface breaking flaw under tension and the results compared against results published by Raju and Newman [20]. This same problem was used to verify the J-integral capability in Grizzly, as documented in [15]. There is very good agreement between the Grizzly interaction integral results and the Raju and Newman values except for at the free surface and at the symmetry plane where there is an issue to be resolved. During the next year, the mode-I integral will be further tested and benchmarked, followed by similar work on the mode-II and III integrals. This will provide the framework for a complete analysis of mixed-mode effects on arbitrary flaw geometries in Grizzly.

2.3 Summary and Future Work

The following developments to the engineering-scale fracture capability in Grizzly have been completed in FY 2014:

1. The J-Integral evaluation capability in Grizzly has been extended to 3D, and the ability to evaluate the term that includes the effects of thermal strain gradients has been added. This has been verified against benchmark solutions.

2. The ability to output mode-I stress intensities calculated from the J-Integral, together with fracture

toughnesses based on the ASTM master curve, including embrittlement as calculated using the EONY model, has been developed in Grizzly.

3. A generic global model of a RPV including a stainless steel liner has been developed, and a set of detailed submodels of material surrounding both embedded and surface-breaking axial and circumferential flaws have been developed. These models have been used to demonstrate the ability of Grizzly to perform a deterministic assessment of crack propagation at the locations of postulated flaws in an embrittled RPV under PTS loading conditions.

4. Significant progress has been made toward developing an interaction integral capability, which will permit the calculation of mixed-mode stress intensity factors on flaws. This will be used to assess the susceptibility of fracture at flaws of arbitrary orientation.

In FY 2015, work will continue to verify and benchmark these capabilities, and demonstrate the usage of these capabilities for assessing fracture susceptibility of RPVs containing flaws of arbitrary orientation.

3 Constitutive Modeling of Ductile to Brittle Transition of Fracture Toughness in Reactor Pressure Vessel Steels

3.1 Introduction

The fracture properties of Reactor Pressure Vessel (RPV) steels show large variation with temperature. Cleavage fracture with limited crack tip plasticity is typically observed at lower temperatures, and is associated with low fracture toughness values (lower shelf). At higher temperatures, ductile fracture due to void nucleation, growth and coalescence is the dominant mechanism. Significant, stable crack propagation occurs prior to final failure, which increases the fracture toughness values substantially (upper shelf). In the transition regime between the lower and upper shelves, unstable cleavage fracture is preceded by ductile damage. Also, large scatter in the fracture toughness values can be observed owing to the inherent statistical nature of cleavage fracture. Irradiation induces additional lattice defects, which reduces the ductility of the material and hence increases the ductile to brittle transition temperature (DBTT). Such irradiation-induced embrittlement of the pressure vessels in light water reactors increases their failure probability and can limit the life extension of the existing fleet. Hence, the development of models considering the influence of irradiation on the fracture behavior of RPV steels is necessary to accurately determine the maximum operational life of the light water reactors.

The master-curve approach is typically used to obtain the DBTT in steels [17, 18]. It is based on fitting the experimentally obtained scattered fracture toughness data with the modified Weibull distribution function

$$P_f = 1 - \exp\left[-\left(\frac{K_J - 20}{K_0 - 20}\right)^4\right] \tag{3}$$

$$K_{JC}(T) = 30 + 70\exp\left[0.019\left(T - T_0\right)\right] \text{MPa}\sqrt{m} \tag{4}$$

where, P_f, K_0, and T_0 are the cumulative failure probability, 63^{rd} percentile fracture toughness value and the DBTT, respectively. The temperature that provides a median fracture toughness (Eq. 4) of 100 MPa$\sqrt{m}$ is considered as the DBTT. However, the master curve equation is based on small scale yielding and neglects the influence of ductile damage. Hence, the applicability of the master-curve approach is limited near the lower shelf and lower failure probabilities. Also, due to the limited availability of irradiated specimens, the determination of DBTT of the embrittled material using the master-curve approach may not be always feasible. Hence in recent years, a physics-based computational approach has been pursued to characterize the full DBT curve for steels [21, 22]. Ductile damage models [23, 24] in conjunction with weakest link theory [25] based criterion, to predict onset of cleavage fracture [26, 27, 28], are used in this approach. The parameters of the ductile damage and the weakest link theory based models are calibrated from fracture tests at a temperature on the upper and lower shelf, respectively and are assumed to remain constant. The temperature dependent flow stress behavior is then used to predict the probabilistic fracture toughness/energy values in the transition regime. This approach has been used to predict the DBTT of unirradiated steels and satisfactory agreement with experiments could be obtained.

In the physics-based computational approach, only stable crack propagation is modeled assuming homogeneous properties and the predicted fracture toughness values are used to assess the integrity of the RPV. However, through thickness variations in radiation damage and temperature in the RPV can cause a heterogeneous distribution of flow and damage properties, which may require modeling of crack propagation after cleavage initiation as well. Hence, a cohesive zone model (CZM) has been developed in FY2013 that captures both stable and unstable crack propagation [29]. The CZM parameters are considered to be dependent on the temperature, irradiation dose and failure probability, to successfully predict the full DBT curve. Though the CZM parameters can be evaluated from lower length scale models, presently these parameters

are calibrated from experimental fracture toughness data. Fairly good match of DBT with experiments were obtained for 1" thick compact tension (1T-CT) specimens made from low alloy pressure vessel steel. In continuation, the model is applied to predict the DBT for 3-point bend (SEB) specimens made from the same alloy and is observed to capture the DBTT shift successfully.

Two different studies are performed to extend the unified CZM approach to predict the DBTT of the irradiated material. In the first study, the effect of specimen size on the predicted fracture toughness values is investigated. Specimen size influences the fracture behavior by altering (i) the out-of-plane constraint to plasticity and (ii) the probability of finding a critical cleavage initiation site. The sub-size pre-cracked Charpy V-notch (PCCv) specimens are typically used in the surveillance capsules in the RPV to monitor the embrittlement and DBTT shifts [30]. These specimens violate the standard size requirements of fracture toughness tests and hence, the master-curve equation is modified as

$$K_{1T} = K_{min} + \left(K_{JC} - K_{min}\right)\left(\frac{B}{B_0}\right)^{1/4} \tag{5}$$

to obtain the standard one-inch thick (1T) equivalent fracture toughness values and DBTT. In Eq. 5, B is the nominal thickness regardless of the side grooving and $B_0 = 25$ mm is the standard specimen width to ensure plane strain condition. The size corrected master-curve equation (Eq. 5) has been used extensively to obtain the DBTT for a wide variety of steels [31, 32]. However, since the size correction term ignores the effect of constraints, its accuracy is restricted near the lower shelf of the transition regime and lower failure probabilities. Detailed numerical investigations using the finite element method (FEM) in conjunction with ductile damage and weakest link theory based models substantiates this observation [33, 34, 35]. Hence, to ensure proper transferability of fracture toughness values from sub-size samples to life assessment of structures, different correction techniques, such as g-function [35], has been proposed. In the present work, a numerical study is performed using CT specimens of different thicknesses to investigate the workability of the unified CZM to capture the size effect on fracture toughness. Comparisons are also made with the traditional approach using the ductile damage model proposed by Gurson-Tvergaard-Needleman (GTN) [36, 37] and Beremin model [27].

In the second study, the influence of irradiation on the flow stress and ductile damage behavior of RPV steels is investigated. Irradiation can cause the formation of vacancy and solute atom clusters, SIA type dislocation loops and precipitates [38]. Initially these loops obstruct the motion of network dislocations that increases the yield stress of the irradiated material. However, beyond a critical stress, the gliding dislocations absorb the loops or loop coarsening and coalescence occurs which create defect-free bands or channels. The formation of these defect-free bands is able to explain the reduction in strain hardening capacity and immediate softening after yield, in highly irradiated RPV steels [39]. For the ductile damage behavior, an increase in the void volume fraction and nucleation rate with irradiation has been assumed in [40] to explain the corresponding decrease in the upper shelf energy. This assumption has been rationalized based on weakening of inclusion interfaces due to phosphorous segregation [41], since irradiation induced defect sizes are too small to influence the void nucleation mechanism [42, 43]. The purpose of the present study is to confirm these assumptions and obtain trends that can reduce the recalibration effort for the irradiated material.

The organization of the chapter is as follows. In Section 3.2 the validation of the unified CZM for SEB specimens is presented. The workability of the unified CZM to capture the effect of specimen size on the fracture toughness is described in Section 3.3. In Section 3.4, the influence of irradiation on the flow stress and ductile damage behavior of RPV steels is investigated. The chapter is concluded in section 3.5.

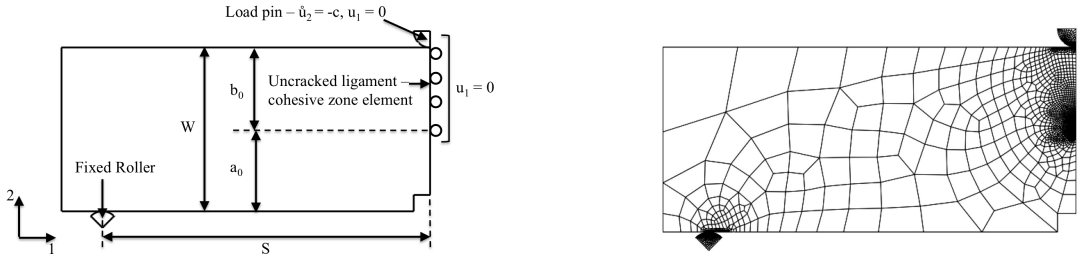

Figure 7: The SEB specimen: (a) Schematic of the geometry and boundary conditions for the 2D FEM simulations. The dimensions W=50 mm, a0=26.1 mm, b0=23.9 mm and S=2W are used, consistent with [1]. Contact elements are used between the load pin, fixed roller and the sample. (b) The FE mesh of the specimen.

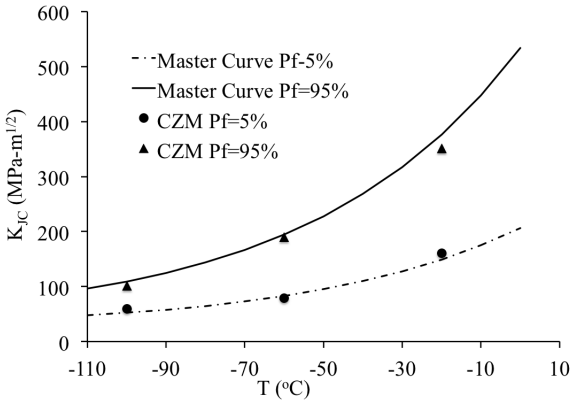

Figure 8: Comparison of fracture toughness between CZM based plane-strain FEM simulations and experiments for the SEB specimen.

3.2 Validation of the Unified Cohesive Zone Model using SEB specimens

The unified CZM model is used to predict the DBT of the one-inch thick single edge notched 3-point bend (SEB) specimen made from low alloy pressure vessel steel [1]. The flow stress and the CZM parameters calibrated from 1T-CT specimens are utilized [29]. The fracture simulations are performed at 3 different temperatures (T=-100°C, -60°C and -20°C) for P_f of 5% and 95%. A schematic of the SEB specimen and the associated FEM mesh is shown in Fig. 7. The quasi-static loading rate (10^{-3} mm/s) and viscosity parameter used in [29] is considered in these simulations.

A comparison of the fracture toughness values obtained from the FEM simulations is made with the master-curve fitted to experiments and is shown in Fig. 8. Similar to the 1T-CT specimen analysis, significant stable crack growth is observed at T=-20°C for P_f of 95%, and the J-integral calculations [44] in conjunction with ASTM 1820 [45] is utilized to obtain the fracture toughness value. A comparison of the fracture toughness values obtained for both the specimen type is shown in Fig. 9. As can be observed from the figure, the SEB specimens have a higher propensity for ductile fracture than the CT specimen at the same temperature. This behavior is due to the higher compliance of the SEB specimens than the CT specimens for the same deep crack geometry (a/W = 0.522), which results in a lower in-plane constraint and higher ductility. This observation is also consistent with experiments as shown in Fig. 9.

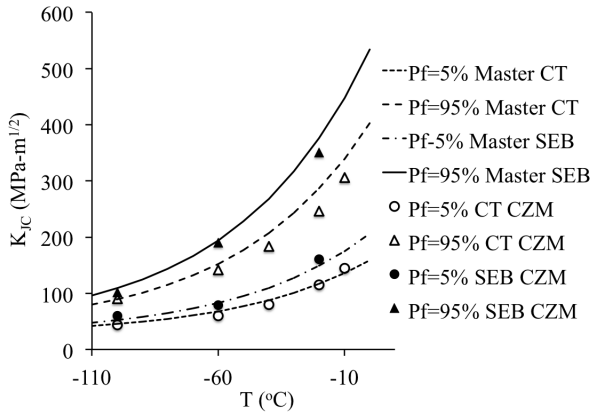

Figure 9: Comparison of fracture toughness between 1T CT and SENB specimen obtained from experiments and CZM based plane-strain FEM simulations.

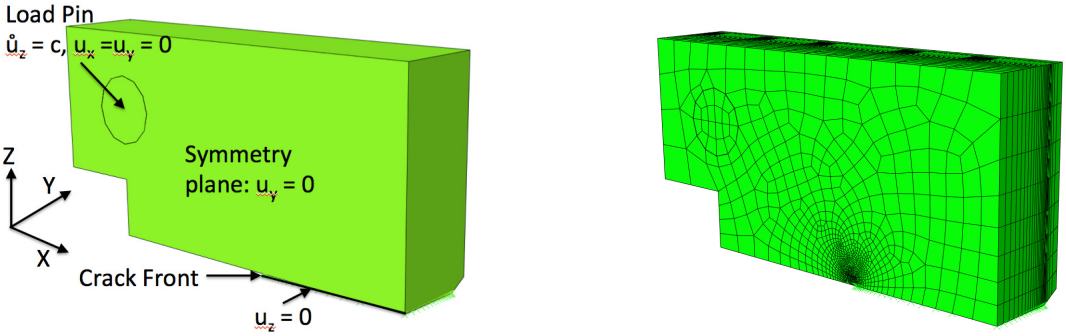

Figure 10: The CT specimen: (a) Quarter symmetry FEM model and boundary conditions. Contact elements are used between the load pin and the sample. (b) The FE mesh of the specimen.

3.3 The effect of specimen size on fracture toughness

To investigate the effect of specimen size on the fracture toughness values and the associated scatter, CT specimens with 3 different thicknesses, B=12.5 mm, 25 mm and 50 mm, are considered. The $a/W = 0.522$ and $B/W = 0.5$ ratios are held fixed where a is the pre-fatigue crack tip and W is the width of the specimen. A side notch is introduced in the model conforming with ASTM standard [45] to maintain a straight crack front. The quarter symmetry FEM model and the mesh of the specimen are shown in Fig. 10. The same mesh size is maintained near the crack-tip for the different crack geometries. The flow stress and calibrated parameter values at T=-100°C is used to perform the FEM simulations.

In the first study, the Beremin model in conjunction with J_2 plasticity is used to obtain the variation of fracture toughness with thickness for cumulative failure probabilities $P_f = 5$ and 95 %. The load-displacement curves and the predicted load at cleavage initiation for $P_f = 5$ and 95 % for the 3 thicknesses is shown in Fig. 11.

The variation of fracture toughness with thickness predicted by the model is shown in Fig. 12. To obtain the fracture toughness values, the relation

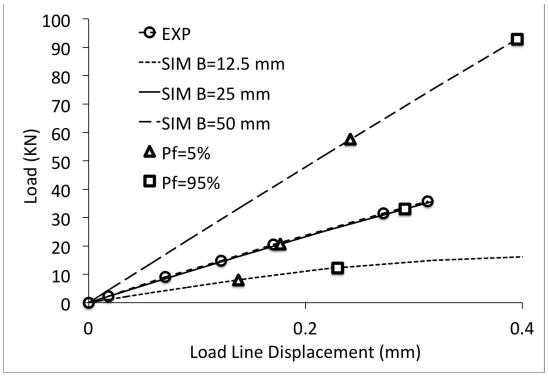

Figure 11: Comparison of the load-displacement curves for different thicknesses with experiment. The load at cleavage initiation predicted from the Beremin model for $P_f = 5$ and 95 % is also shown.

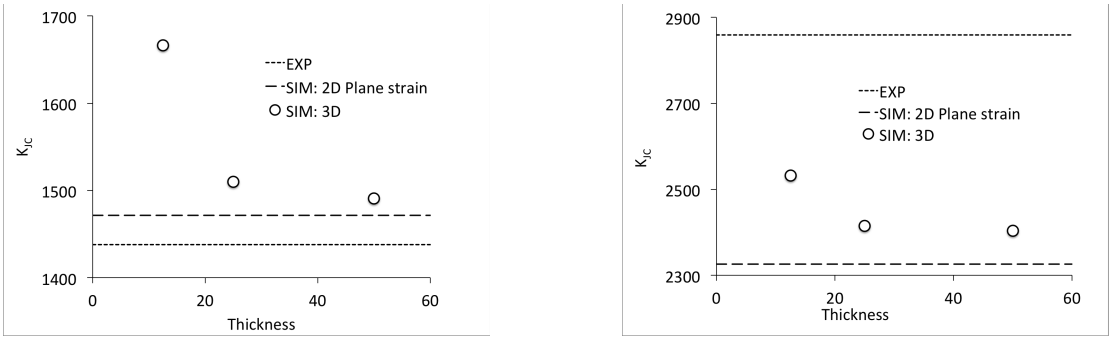

Figure 12: Thickness effect on fracture toughness (K_{JC}) obtained using Beremin model and J_2 plasticity at T=-100°C: (a) $P_f = 5$ % and (b) $P_f = 95$ %.

$$K = \frac{P}{B\sqrt{W}} f\left(\frac{a}{W}\right) \text{ where}$$
$$f\left(\frac{a}{W}\right) = \frac{2+\frac{a}{W}}{\left(1-\frac{a}{W}\right)^{3/2}}\left[0.886 + 4.64\left(\frac{a}{W}\right) - 13.32\left(\frac{a}{W}\right)^2 + 14.72\left(\frac{a}{W}\right)^3 - 5.6\left(\frac{a}{W}\right)^4\right] \quad (6)$$

based on small scale yielding has been used [46] in which P is the load at cleavage initiation obtained from the Beremin model. In Fig. 13, a comparison of the analytical scaling relation (Eq. 5) is made with the predicted fracture toughness values. As can be observed from the figure, a good correlation with Eq. 5 is only obtained at $P_f = 5$ % and thickness of 12.5 mm. Overall the size effect as predicted from the model has less variation than the analytical form. However a similar trend, viz. increased fracture toughness with thickness reduction, can be obtained.

The unified CZM is then used to predict the influence of specimen thickness on the fracture toughness. With decreasing thickness, the amount of ductile damage prior to cleavage initiation increases due to more crack-tip plasticity and hence the fracture toughness increases. This behavior can be captured using CZM and is evident from the load-displacement curves obtained from CZM based FEM simulations under plane strain and stress conditions shown in Fig. 14.

However, the statistical effect of thickness is absent in the unified CZM and hence it may not capture the desired variation particularly near the lower shelf and lower failure probabilities, where constraint effects are

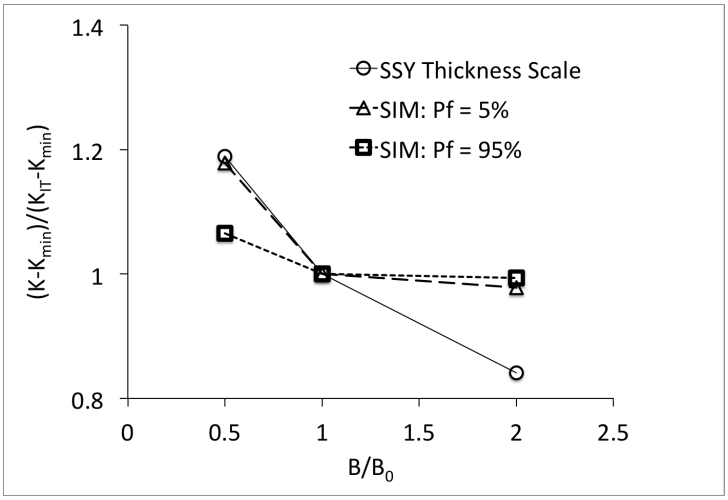

Figure 13: Comparison of the load-displacement curves for different thicknesses with experiment. The load at cleavage initiation predicted from the Beremin model for (P_f) = 5 and 95 % is also shown.

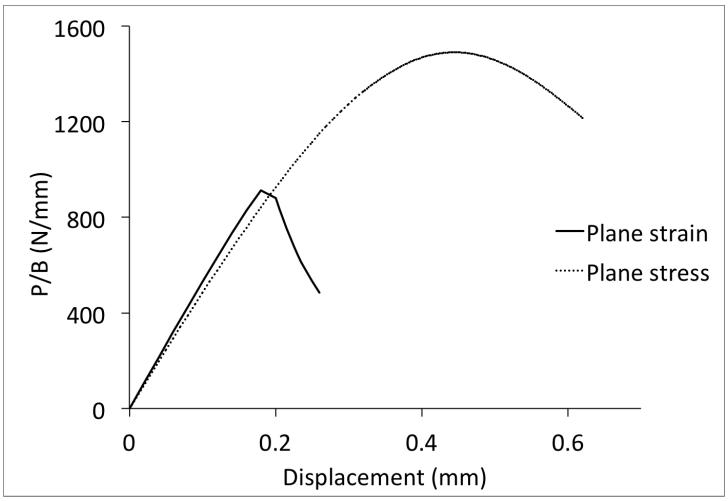

Figure 14: The load-displacement evolution under plane stress and strain conditions obtained from unified CZM based FEM simulations. The cohesive parameters corresponds to T=-100°C and P_f = 5 %.

minimal. To substantiate this fact, unified CZM simulations of the CT specimen is performed considering different thicknesses. The CZM parameters calibrated from the 1T CT specimen at T=-100°C and P_f = 5 % are used. A comparison of the load-displacement for different thicknesses is shown in Fig. 15. Subsequently fracture toughness values are evaluated using Eq. 6 and is shown in Fig. 16. As can be observed from the figure, the unified CZM in its present form is unable to capture the influence of specimen thicknesses on the fracture toughness particularly near the lower shelf and lower failure probabilities. In a 3D context, developing a damage surface for the CZM considering the shear stresses may partially negate the reverse trend observed in this case. However considering the statistical variation of cohesive properties along the thickness is still necessary.

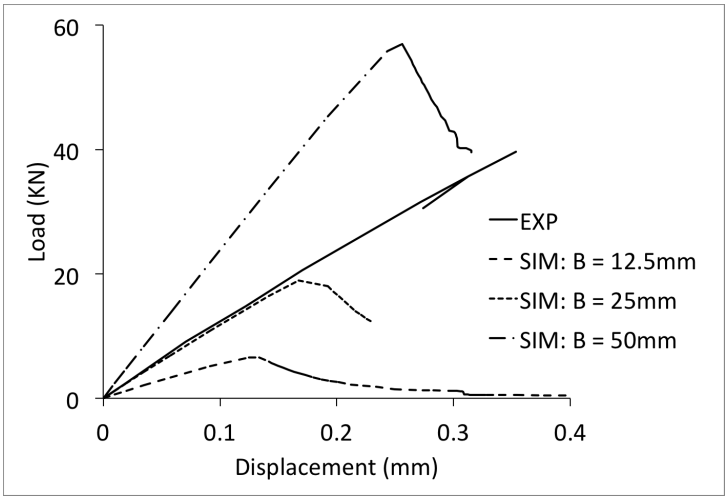

Figure 15: The load-displacement evolution obtained from unified CZM based FEM simulations of CT specimens with different thicknesses. The cohesive parameters obtained at T=-100°C and $P_f = 5$ % is used.

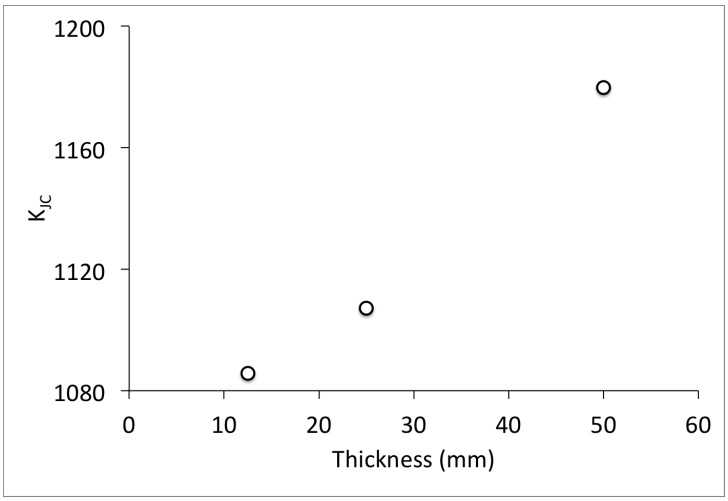

Figure 16: The variation of fracture toughness with thickness obtained at T=-100°C and $P_f = 5$ %.

3.4 Characterization of irradiation effects on the ductile damage and flow stress behavior

A numerical sensitivity study has been performed to relate the influence of irradiation on the ductile damage and flow stress model parameters in RPV steels. The tensile data of T91 and EUROFER97, irradiated at 300°C to different dose levels and tested at the same temperature is considered [47]. Though both these alloys have the same Cr content (9 wt %), the differences in the wt% of P, Mo and Ni cause significant dissimilarity in their stress-strain behavior. A comparison of the chemical compositions of the 2 alloys is shown in Table 1. Both the alloys have a tempered ferritic/martensitic (F/M) microstructure with similar martensitic lath structure as observed from TEM images of the unirradiated specimens [47]. Carbides of type $M_{23}C_6$ are found on grain/sub-grain boundaries in both these alloys with the same size distribution. However, the differences in prior austenitic grain size, carbide distribution and dislocation structure is hypothesized to cause the variations in stress-strain evolution and ductility in these alloys. After irradiation, T91 is observed to have smaller and more homogeneously distributed defect loop structure than EUROFER97 and hence shows

Table 1: Chemical composition of T91 and EUROFER97 (wt%).

Steel	Cr	C	Mo	W	Ta	V	Mn	Ni	Si	Nb	P
T91	8.32	0.1	0.96	<0.01		0.24	0.43	0.24	0.32	0.06	0.02
E97	8.96	0.12	<0.001	1.1	0.13	0.19	0.43	0.007	0.07	<0.001	<0.005

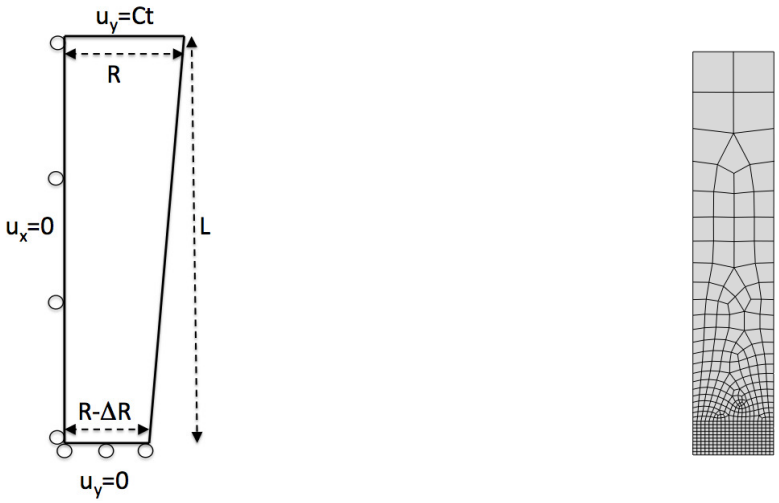

Figure 17: (a) Schematic of the axisymmetric FE model and boundary conditions. L = 6 mm, R = 1.2 mm and ΔR/R = 0.4% and 0.8% is used to perform the simulations. (b) FE mesh using 8-node quadrilateral elements with reduced integration. A mesh size of 0.06 mm is used at the necking region.

higher ductility for the same dose level [47]. Though the F/M steels have a different chemical composition and microstructure than the RPV steels, their stress-strain behavior shows a similar sensitivity to irradiation [48, 49] and hence the conclusions made in this study are extended to RPV steels.

3.4.1 Flow stress, ductile damage and FEM model

The tensile experiments of T91 and EUROFER97 have been performed on cylindrical specimens with diameter = 2.4 mm and gauge length = 12 mm. An axisymmetric FEM model with the same dimensions is used to perform the analyses and is shown in Fig. 17. To introduce necking in the specimens, a small radial offset (0.4%) is introduced on the outer edge at the centerline similar to [37] as shown in Fig. 17(a). The radial offset incorporates the effect of full specimen geometry and defects that can cause heterogeneous stress distribution and necking. The 8-noded isoparametric element with reduced integration is used for discretizing the specimen geometry (Fig. 17(b)).

The constitutive behavior of the specimen is characterized using the rate independent ductile damage model developed by Gurson [24] and later modified by Tvergaard and Needleman [36, 37]. In this model, following large deformation theory, the plastic component of rate of deformation tensor, $\mathbf{D^p}$, is represented by:

$$\mathbf{D^p} = \dot{\lambda}\frac{\partial \phi}{\partial \boldsymbol{\sigma}} \tag{7}$$

The flow potential ϕ in Eq. 7 is defined by

$$\phi = \frac{\sigma_e^2}{\sigma_m^2} + 2f^* q_1 \cosh\left(\frac{q_2 \sigma_h}{2\sigma_m}\right) - 1 - q_1^2 f^{*2} \tag{8}$$

and the flow rate $\dot{\lambda}$ is obtained from the equivalence of plastic power using

$$\dot{\lambda} = \frac{(1-f)\,\sigma_m \dot{\epsilon}_m}{\boldsymbol{\sigma} : \partial\phi/\partial\boldsymbol{\sigma}} \tag{9}$$

In Eqs. 8 and 9, σ_e is the Von Mises stress, σ_h is the hydrostatic stress, σ_m and ϵ_m is the flow stress and plastic strain in the un-voided matrix respectively, f^* is the modified void volume fraction and q_1, q_2 are parameters that accounts for the pressure sensitivity. The flow stress behavior is represented using the Ramberg-Osgood equation with an additional exponential term as

$$\sigma_m = \sigma_0 \left(\frac{E\epsilon_m}{\sigma_0} + 1\right)^n + C_0 + C_1 exp\left(\left(\frac{\epsilon_m}{|\epsilon_r|}\right)^m sgn\left(\epsilon_r\right)\right) \tag{10}$$

where σ_0, E, n and ϵ_r are the yield stress, Young's modulus, flow exponent and a reference strain-type value, respectively. A negative or positive value of ϵ_r is used to incorporate strain softening or additional hardening, respectively. The parameters C_0, C_1 and m in Eq. 10 control the amount of softening or additional hardening in the material. Similar functional form has been used in [48] to capture the early necking behavior observed in irradiated bcc iron.

The modified void volume fraction (f^*) in Eq. 8 considers the accelerated growth and coalescence of voids (f) once the critical volume fraction (f_c) is exceeded, and is expressed by

$$f^* = \begin{cases} f, \text{ for } f \le f_c \\ f_c + \dfrac{f_u - f}{f_f - f_c}, \text{ for } f > f_c \end{cases} \tag{11}$$

where $f_u = 1/q_1$ and f_f is the final void volume fraction. The evolution of f is governed by the growth of the existing voids, f_g, and additional void nucleation, f_n, as

$$\dot{f} = \dot{f}_g + \dot{f}_n \tag{12}$$

The growth rate of f_g is defined as

$$\dot{f}_g = (1-f)\,\mathrm{tr}\left(\boldsymbol{D}^p\right) \tag{13}$$

and a strain controlled void nucleation rate is considered

$$\dot{f}_n = \frac{f_N}{s_N\sqrt{2\pi}} \exp\left(-\frac{1}{2}\left(\frac{\epsilon_m - \epsilon_N}{s_N}\right)^2\right) \tag{14}$$

where f_N, s_N and ϵ_N are the parameters that represent the statistical nature of void nucleation. A normal distribution is considered where ϵ_N and s_N represents the mean and standard deviation respectively. The model is numerically integrated using the backward Euler scheme described in and is implemented into ABAQUS utilizing the UMAT subroutine [50].

Table 2: Flow stress parameters (Eq. 10) of T91.

dpa	E (GPa)	σ_0	n	C_0	C_1	m	ϵ_r
0	210	464	0.084	-	-	-	-
0.06	210	502	0.092	-	-	-	-
0.6	210	645	0.066	-	-	-	-
1.5	210	715	0.05	-	-	-	-

Table 3: Calibrated ductile damage model parameters of T91.

f_c	f_f	f_N	ϵ_N	s_N	q_1	q_2
0.05	0.25	0.01	0.08	0.02	1.0	1.0

3.4.2 Results and Discussions

The tensile data of T91 is considered first for the numerical study. The flow stress parameters (Eq. 10) are obtained by performing a least square fit of the true stress-strain curve till ultimate tensile strength and is shown in Table 2. A sensitivity study is then performed to determine the ductile damage parameters of the unirradiated specimen and is shown in Table 3. A comparison of the engineering stress-strain behavior with experiment and the evolution of void volume fraction at the center of the specimen are shown in Fig. 18. As can be observed from the figure, the calibrated flow stress and ductile damage model parameters provide a satisfactory agreement of stress-strain evolution with experiments. In Fig. 19, the distribution of equivalent stress, plastic strain and void volume fraction in the failed sample is shown.

For the irradiated specimens, a reduction in the uniform and total elongation with increasing dose-level is observed. This behavior can occur due to surface defects in the specimens introduced by radiation damage. This assumption is verified by comparing the simulated stress-strain evolution with experiments (Fig. 20) after increasing the radial offset in the irradiated specimens from 0.4 to 0.8%. In these simulations, the flow stress and ductile damage parameters shown in Tables 2 and 3 are used respectively. As can be observed from Fig. 20, the experimentally obtained stress-strain curves can be satisfactorily reproduced without modifying the ductile damage model parameters and by incorporating the influence of specimen defects. A comparison of the yield strength, ultimate tensile strength, uniform and total elongation with the experimental values is shown in Fig. 21. These results suggest that the ductile damage model parameters are not affected by irradiation in this alloy.

Similar to T91, the ductile damage model parameters for EUROFER97 are calibrated using the tensile data of the unirradiated specimen. However for this alloy, the Ramberg-Osgood power law hardening is found to be insufficient and the additional exponential term in Eq. 10 is required to describe the flow stress behavior. The parameters for the Ramberg-Osgood equation are obtained from a least square fit of the true stress-strain curve till ultimate tensile strength while the other parameters are obtained from a sensitivity study and are listed in Tables 4 and 5 respectively. A comparison of the engineering stress-strain behavior with the experiment and the evolution of the void volume fraction at the center of the unirradiated specimen are shown in Fig. 22. For the specimens irradiated to dpa = 0.6 and 1.5, uniform elongation is almost absent. For these cases the flow stress parameters are calibrated from the experimental stress-strain curves while keeping the ductile damage model parameters fixed and is shown in Fig. 23. A comparison of the yield strength, ultimate tensile strength, uniform and total elongation with the experimental values is shown

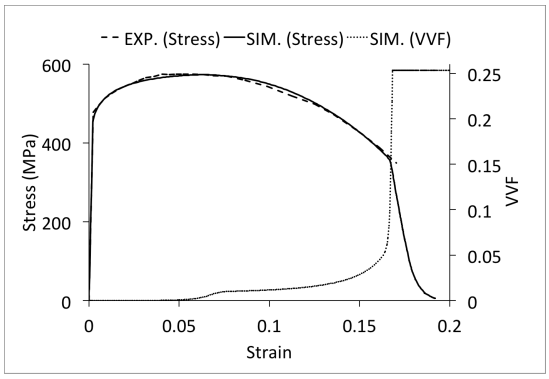

Figure 18: Comparison of engineering stress-strain between FE simulation and experiments for T91. The evolution of void volume fraction (VVF) in a material point at the specimen center is also shown.

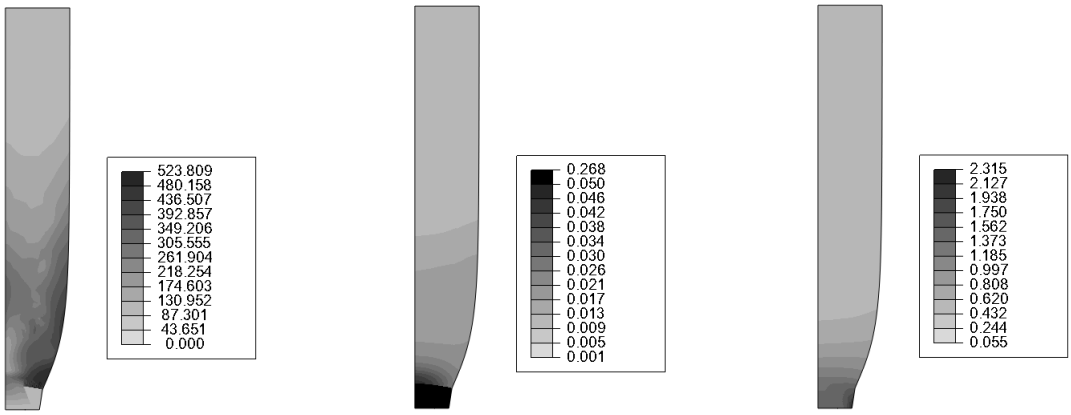

Figure 19: Distribution of (a) Von Mises stress (b) void volume fraction (c) equivalent plastic strain in the specimen (T91) after failure.

in Fig.24. As can be observed from the figures, irradiation has no influence on the ductile damage model parameters and only affects the flow stress behavior in this alloy. The reduction in area after complete failure in T91 and EUROFER97 are compared in Fig. 25. For the unirradiated EUROFER97 specimen tested at T=300°C, the predicted reduction of area (80%) compares well with the experimental values [51].

The chemical composition of RPV steels is different from the F/M steels considered in this work and is

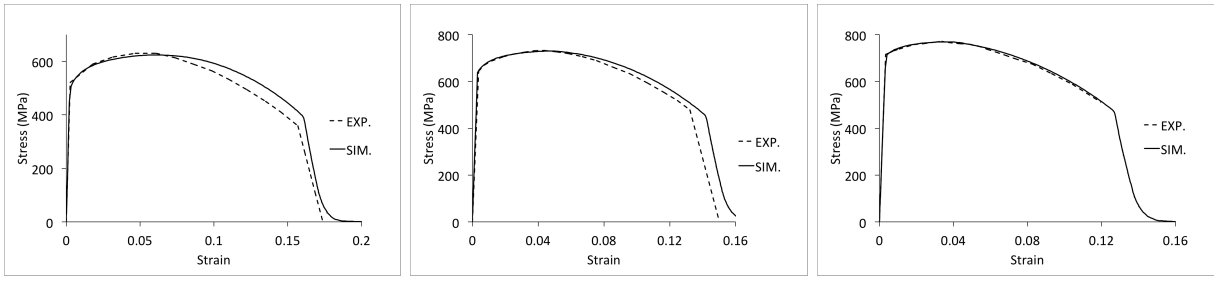

Figure 20: Comparison of engineering stress-strain between FE simulation and experiments for T91 irradiated to (a) dpa = 0.06 (b) dpa = 0.6 (c) dpa = 1.5.

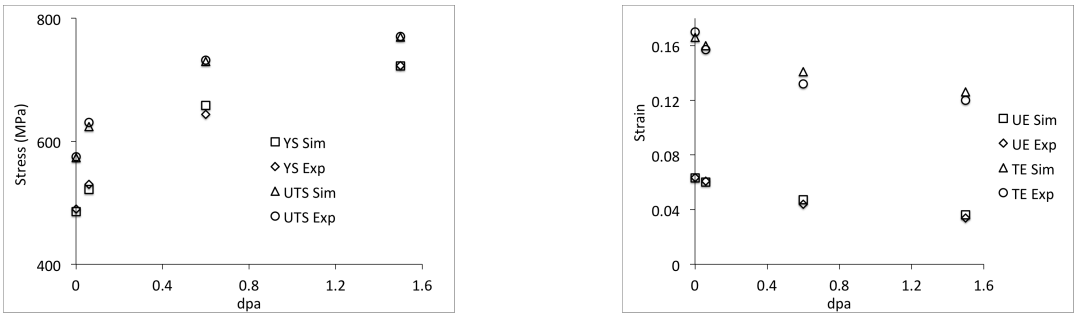

Figure 21: Comparison of (a) yield (YS) and ultimate tensile strength (UTS), (b) uniform (UE) and total elongation (TE), between FE simulation and experiments for T91.

Table 4: Flow stress parameters (Eq. 10) of EUROFER97.

dpa	E (GPa)	σ_0	n	C_0	C_1	m	ϵ_r
0	210	495	0.05	0.0	20.0	0.75	0.4
0.06	210	515	0.042	0.0	20.0	0.75	0.4
0.6	210	650	0.03	-40.0	40.0	1.0	-0.01
1.5	210	725	0.01	-50.0	50.0	1.0	-0.01

shown for the "JRQ reference steel" [52] in Table 6. A comparison of the chemical composition with T91 (Table 1) reveals that these alloys have: a lower Cr, V content; higher Mn, Ni and Cu content; and similar C, Mo and P content. Long-term exposure of these steels to irradiation results in the formation of small (few nanometers) vacancy clusters, SIA loops; Cu, Ni, Mn, C precipitates and possible segregation of P on grain boundaries. These defects impede the motion of dislocations and increase the yield stress of the irradiated material similar to F/M steels. At higher irradiation doses, loss of strain hardening capacity is also observed in these steels due to the formation of defect free bands [49]. Hence similar to F/M steels, irradiation can influence the ductile damage behavior of RPV steels by altering the flow stress behavior that affects the void growth rate, as observed in this study. However, the damage nucleation in RPV steels remains insensitive to irradiation.

Table 5: Calibrated ductile damage model parameters of EUROFER97.

f_c	f_f	f_N	ϵ_N	s_N	q_1	q_2
0.2	0.4	0.02	0.03	0.01	1.0	1.0

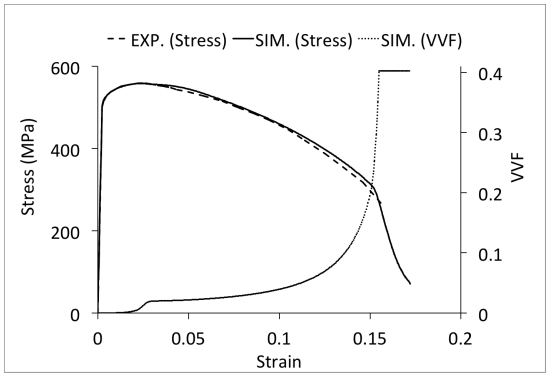

Figure 22: Comparison of engineering stress-strain between FE simulation and experiments for EUROFER97. The evolution of void volume fraction (VVF) in a material point at the specimen center is also shown.

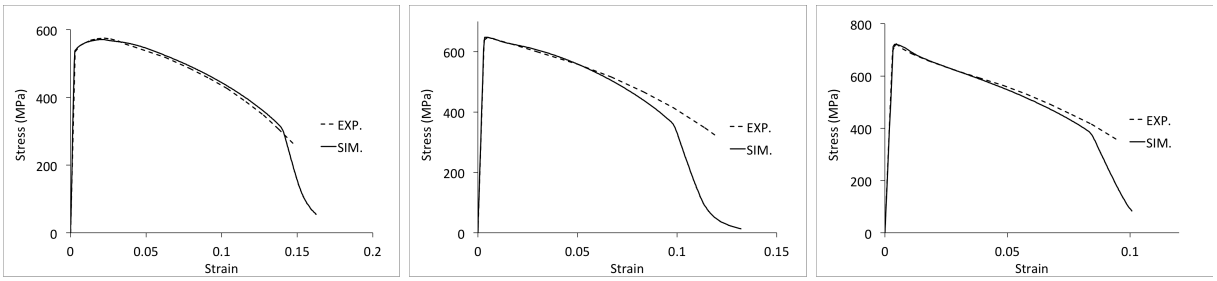

Figure 23: Comparison of engineering stress-strain between FE simulation and experiments for EUROFER97 irradiated to (a) dpa = 0.06 (b) dpa = 0.6 (c) dpa = 1.5.

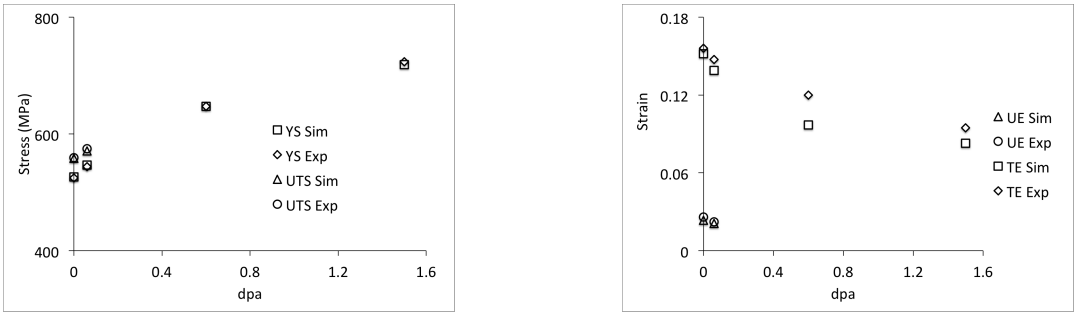

Figure 24: Comparison of (a) yield (YS) and ultimate tensile strength (UTS), (b) uniform (UE) and total elongation (TE), between FEM simulation and experiments for EUROFER97. The UTS and UE at dpa = 0.6 and 1.5 is not shown in the figure since there is negligible uniform elongation at these dose levels.

Table 6: Chemical composition of JRQ reference steel (wt%).

C	Si	Mn	P	S	Cu	Ni	Cr	Mo	V	Al_{sol}
0.18	0.24	1.42	0.017	0.004	0.14	0.84	0.12	0.51	0.002	0.014

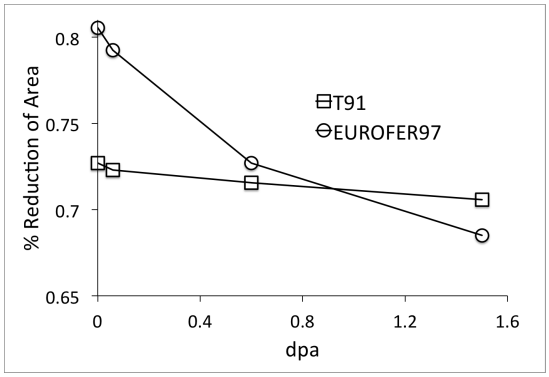

Figure 25: Comparison of % reduction of area with irradiation dose level between T91 and EUROFER97.

3.5 Summary and Future Work

In summary, the following investigations have been performed at the specimen scale to support the Grizzly project in FY 2014:

1. The workability of the unified CZM developed in FY 2013 has been verified using SEB specimens of the same material. From a comparison of the fracture toughness with the master-curve it is observed that the model is able to capture the DBTT shift occurring due to specimen geometry effect.

2. The specimen size effect on DBTT has been investigated using the conventional approach with J_2 plasticity and Beremin model, as well as the unified CZM. The conventional approach is able to capture the increasing trend with reducing thickness though an exact match with the analytical equation has not been obtained. The unified CZM incorporates the constraint effect as observed from the 2D simulations but fails to capture the statistical variations in cleavage strength due to specimen thickness particularly near the lower shelf and lower failure probabilities.

3. From a numerical sensitivity study on tensile specimens using the ductile damage model it is shown that irradiation has a strong influence on the flow stress behavior which alters the ductile damage growth. However, void nucleation is observed to be insensitive to irradiation.

In FY 2015, a microstructure-scale crystal plasticity model will be developed to capture the effect of irradiation on the flow stress behavior. This model can consider the presence of defects on particular slip systems and their interactions with glide dislocations in a phenomenological way to provide macroscopic flow stress behavior. Initially a qualitative analysis of sensitivity of flow stress to radiation damage will be made for RPV steels. However, with the availability of quantitative estimates of defect cluster size distributions and their interaction strengths from lower length scale models, realistic predictions can be obtained. Validation of the model will be performed based on the availability of experimental data.

4 Microstructure evolution in RPV steels: Solute precipitation and defect evolution in RPV steels

4.1 Introduction

The integrity of reactor pressure vessels (RPVs) is one of the primary safety factors that limit the service life of current LWRs [9, 2]. In these reactors, RPVs are made of low-alloy steels with Mn, Ni, C and Si being the primary alloying elements, and Cu being either an alloying element or an impurity. During service, RPVs are subject concurrent thermal aging at high temperature and fast neutron irradiation. Consequently, the microstructure of RPV steels evolves by precipitation of alloying elements and accumulation of irradiation-induced lattice defects. The formation of Cu-rich-precipitates (CRPs) is one of the main contributors to RPV embrittlement. At high neutron fluence, another type of precipitates, the Mn/Ni rich precipitates (MNPs) or the so-called late-blooming phase [10], may also form in low to no Cu alloying steels, adding some uncertainty on the RPV embrittlement during extended service life. In addition to solute precipitation, building-up of irradiation-induced lattice defects (or matrix features) acts as another primary factors for RPV hardening and embrittlement since both precipitates and lattice defects can impede dislocations. Due to the slow kinetics involved, these effects may take several or tens of years to develop, making experimental studies difficult. Alternatively, science-based predictive modeling with validations using the limited experimental data [12] has become a promising approach to evaluate RPV embrittlement.

In this chapter, the effort taken in FY 2014 to address the solute precipitation and structural evolution of irradiation-induced matrix features will be presented. We start with further development of the atomic-kinetic-Monte-Carlo (AKMC) [14] method to describe the effect of solute trapping, and then proceed with the development of a phase field model to model solute precipitation over a large time and length scale. Some simulation results will also be presented in the Results section followed by the Summary.

4.2 Method development

4.3 Atomic Kinetic Monte Carlo

RPV steels are low alloying steels usually with the tempered bainitic microstructure, which consists of dislocation-rich ferrite and cementite. In both modeling and experiments, ferritic model alloys with the body-center-cubic (bcc) crystal structure have been widely used to investigate the solute precipitation during both thermal aging and neutron irradiation. In FY 2013, an AKMC model has been developed using the SPPARKS framework [53] under the Grizzly project. The model is capable of modeling diffusion and precipitation of solute elements including Cu, Ni, Mn, and Si within a bcc Fe matrix [54] under thermal aging conditions. In that model, solute atoms diffuse via switch with vacancies, either thermal or irradiation produced ones. The effects of irradiation-induced matrix features, such as voids and prismatic loops, have also been elucidated using molecular dynamics (MD) and Metropolis-Monte-Carlo (MMC) simulations. The results have been summarized into a journal article which is currently under review [55]. The effects of matrix features such as dislocations and prismatic loops on solute precipitation have also been incorporated into the AKMC model via elastic interaction.

The AKMC simulations predict the number density and size distribution of precipitates as functions of time. The current AKMC model adopts the residence-time-algorithm where the KMC time t_{KMC} is given by the switch of vacancies with surrounding atoms [14]. To convert the KMC time to realistic time, two factors need be considered. First, the vacancy concentration in an AKMC simulations is different from, usually order higher than that in reality. Second, in AKMC simulations a constant vacancy concentration is used and in a large amount of time the vacancies are trapped by the solute precipitates. However in reality, only vacancies in the Fe matrix contribute to time advancement. This effect is called solute trapping and has to be taken

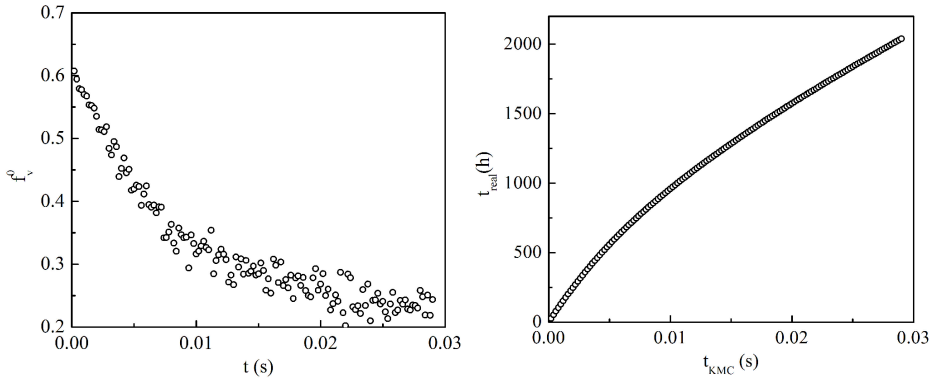

Figure 26: (a) Fraction of time vacancies spent in the Fe matrix and (b) realistic time as functions of KMC time in an AKMC simulations at 773 K.

into consideration. To address these issues, we adopted the method used in Soisson et al. [56] where the advancement in realistic time t_{real} is given by $t_{real} = t_{KMC}\frac{f_v^0 C_v^{KMC}}{C_v^{real}}$. Here C_v^{KMC} is the vacancy concentration used in the simulations, and f_v^0 measures the fraction of time vacancies spent in the Fe matrix (sites without Cu atoms being the first or second nearest neighbors). C_v^{real} is the realistic vacancy concentration, such as that in a thermal aging experiments. At finite temperature T, the equilibrium thermal vacancy concentration can be estimated by $C_v^{real} = exp(-\frac{E^f}{KT})$, with E^f being the vacancy formation energy and K Boltzmann constant.

In Fig. 26, the effect of solute trapping in a Fe-Cu1.34% alloy is demonstrated. The simulation cell contains 2 million atoms with 16 vacancies. The parameters given by Vincent et al. [54] are used to define the interatomic interaction, with the bonding energies between vacancies adjusted to give zero binding between them. An attempt frequency of 10^{13}/s is used to evaluate KMC time. The vacancy formation energy is taken to be 1.60 eV to estimate the equilibrium thermal vacancy concentration. As shown in Fig. 26(a), a substantial fraction of the KMC time is due to trapping of vacancies by solute or solute clusters, and the trapping effect increases as the precipitation progresses. Since the vacancy concentration used in the simulations is much higher than the thermal equilibrium concentration at the same temperature, the KMC time actually corresponds to a much longer realistic time, e.g., that in a thermal aging experiments with the same material system at the same temperature, as shown in Fig. 26(b).

4.4 Phase field

The AKMC simulation can directly take input from density-functional-theory (DFT) calculations and MD simulations to give an accurate description on the nucleation and growth of solute precipitates. However, due to the solute trapping, it becomes extremely slow at the later stage of precipitation and thus not applicable for coarsening of precipitates. The length scale of AKMC simulation is also limited by its atomic resolution. Mesoscale method such as phase field is therefore desired to describe solute precipitate at larger time and length scales. This effort has barely started in FY 2014 and the effort is paid to developing a nucleation algorithm for solute precipitates.

In phase field there are primarily two ways treating nucleation of second phases. In the first one, which we call the "Langevin noise approach"[57], the thermal fluctuations which are normally absent from Phase Field models are explicitly added. This results either in stochastic source/sink terms in the Cahn-Hilliard or Allen-Cahn equations, or a post processing of the solution at every time step to modulate the concentration/order parameter fields. In the second approach, which we call "Poisson seeding"[58], the expectation value for the

number of nuclei that should be present in the simulation volume is computed at each time step. According to a Poisson probability distribution seeds are inserted into the simulation cell at random. In FY 2014, an implementation of the Langevin noise approach in MOOSE phase field module has started. We follow the approach of adding the noise as a source/sink term in the Cahn-Hilliard equation. To conserve the total amount of solute in the system the integral over the noise term needs to be zero. For this purpose a new module was added to MOOSE to handle the generation of noise terms that fulfill this restriction, a group of UserObjects derived from the ConservedNoiseBase class.

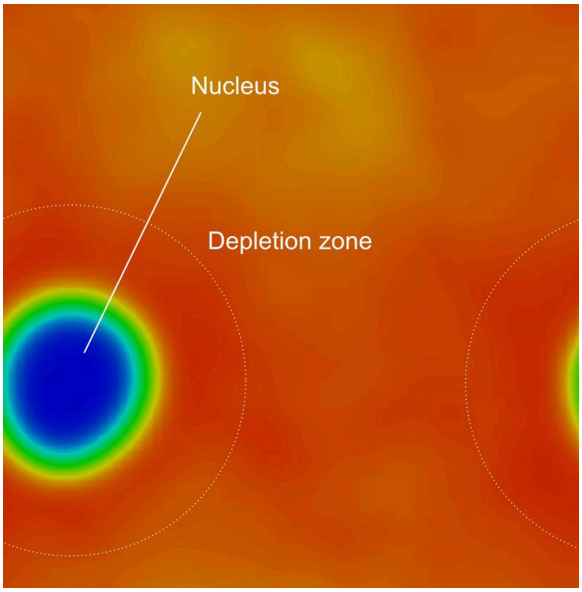

Figure 27: Nucleation of a precipitate in a phase field simulation with an added Langevin noise term. The free energy is a polynomial double well potential and the global solute concentration is outside of the spinodal region. Note the depletion zone around the freshly formed nucleus. The color represents the local solute concentration spanning from 0.0 (red) to 1.0 (blue).

The efficacy of the Langevin noise term has been tested by a phase field simulation simulations using a polynomial double well free energy function. The global solute concentration was set to a spatially uniform value chosen to be outside the spinodal of the system. Nucleation is observed spontaneously. A developing nucleus is shown in Fig. 27 and a solute depleted zone forms naturally around the nucleus. The simulation is done using the MARMOT application [59]. The nucleation capability can also be used in the Grizzly phase field part which is currently under development.

4.5 Results

4.5.1 Precipitation kinetics: Benchmark with thermal aging kinetics

To validate the AKMC model, two simulations with Fe-Cu1.34% alloy at 773 K are performed to benchmark with previous thermal aging experiments. The simulations cells are cubic, 28.5 by 28.5 by 28.5 nm^3 in volume with two million atoms. In the first simulations, the system contains no defects and an edge dislocation is introduce in the other simulation, corresponding to a dislocation density of $1.2*10^{15}/m^2$. Note that this dislocation density is much higher than that in a typical RPV steel, usually in the order of $10^{13}/m^2$. The dislocation is introduced by introducing the corresponding stress field given by the Stroh formalism [60] without representing the exact atomic structure. Cu atoms interact elastically with the stress field by $\Delta E = P\Delta V$,

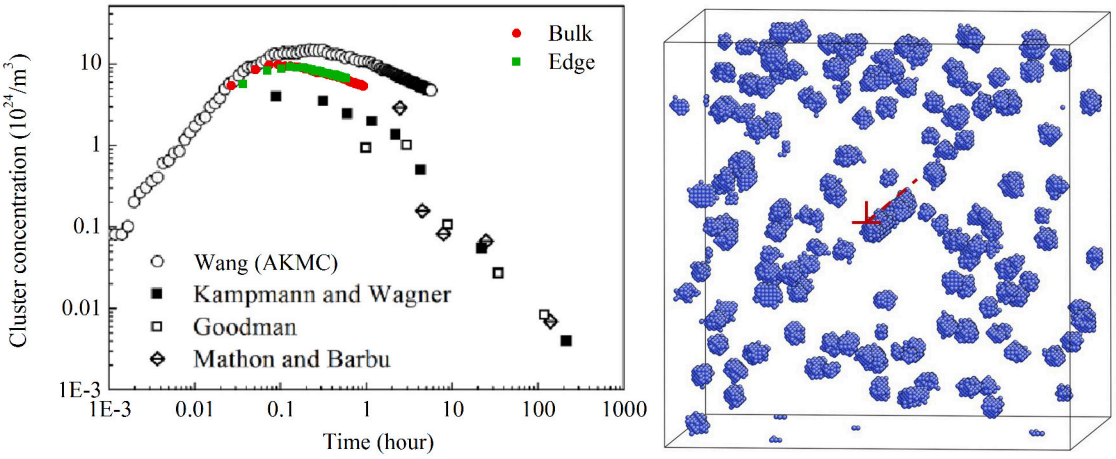

Figure 28: (a) Number density of CRPs as a function of time and (b) precipitate configurations in a simulation cell with an edge dislocation at the center. Decoration of the dislocation line (red dash line) by CRPs is observed with a denuded zone nearby. Blue spheres are Cu atoms. Fe atoms are omitted for clarity.

where P is the local hydrostatic pressure and ΔV is the excess volume of Cu in reference to bcc Fe [55]. The parameters given in Vincent et al. [54] are used in the simulations and an attempt frequency of 10^{13}/s is used for vacancy diffusivity. To estimate the thermal vacancy concentration a vacancy formation energy of 1.60 eV is used. While counting the number density, Cu clusters with more than 10 Cu atoms are taken as precipitates.

As shown in Fig. 28(a), the number density of CRPs first increases showing nucleation and then decreases showing growth and coarsening. In general, the simulation results agree with experimental ones reasonably well. The peak number density given by the AKMC simulations is higher, by a factor of 2-3, than those measured in thermal aging experiments. It is also noticed that introduction of dislocation (edge) does not alter the number density of CRPs very much from that in defect free matrix (bulk). However, the atomic configuration (Fig. 28(b)) indicates a clear decoration of the dislocation line by CRPs. Such heterogeneous Cu precipitation may change the hardening behavior from that given by a mean distribution of CRPs. The current parameters give a good estimate on the time when the peak density of CRPs is obtained. We note that the estimated realistic time is very sensitive to the parameters used including vacancy formation energy, attempt frequency and migration barriers. DFT calculations have been widely used to predict these parameters, with however scattered results in literature [14].

Once the nucleation stage has passed, the effect of solute trapping becomes stronger and stronger. As a result, the time required for an AKMC simulation to advance in realistic time increases substantially, making AKMC simulation not applicable to simulate coarsening behavior. Mesoscale methods such as phase field are needed for this purpose.

4.5.2 Structural transformation of radiation induced defects in bcc Fe

As mentioned earlier, irradiation induced matrix features may also lead to hardening and embrittlement and this effect increases as neutron fluence increases. They may also affect the precipitation kinetics of solute elements. Understanding the accumulation of irradiation-induced matrix features in RPV steels is critical for the assessment of RPV integrity. In the past few decades there have been intensive research interests in irradiation damage in steels or model alloys, however, with a lot of questions still unresolved.

In FY 2014, fundamental studies on the structural evolution of some matrix features have been conducted under the Grizzly project. Specifically, we studied the relative stability between prismatic loops and three-dimensional SIA clusters with the C15 Laves phase (referred to as C15 clusters) using MD simulations and the structural transformation from C15 cluster to loops. This work is motivated by two open questions. The first is the formation mechanism of ⟨100⟩ SIA loops. In bcc Fe, clusters of SIAs are usually observed to take loop configurations with either a ⟨100⟩ or a ⟨111⟩/2 (referred to as ⟨111⟩) Burgers vector [61, 62]. While there is abundant evidence of ⟨100⟩ loop formation, how they actually form remains a puzzle. Not like ⟨111⟩ loops which can nucleate by cluster of ⟨110⟩ dumbbell SIAs with slight rotation, direct nucleation of ⟨100⟩ loops by SIA clustering is highly unlikely due to the high formation energy of ⟨100⟩ dumbbell. A few recent attempts explain the formation of ⟨100⟩ loops by interaction [63, 64] or direct transition [65] of ⟨111⟩ loops. All these mechanisms require pre-existing ⟨111⟩ loops, in contrast to a recent experimental observation showing that at high temperatures, ⟨100⟩ loops can form exclusively without presence of ⟨111⟩ loops [66]. Moreover, special constraints are usually involved in these mechanisms. The second open question is the existence of 3D SIA clusters, or more specifically C15 clusters, in bcc Fe. C15 cluster in bcc Fe has recently been predicted by DFT calculations and they are shown to be even more stable than ⟨111⟩ loops at small size range. However they have never been observed experimentally, leaving their existence another puzzle.

Here, we use MD simulations to address the two aforementioned puzzles and find that they have a close correlation. Relative to ⟨111⟩ and ⟨100⟩ loops, C15 clusters are found to be more stable within a certain size range. Consistently, dynamics simulations demonstrate that C15 clusters can grow by absorbing individual SIAs until they transform into loops at sizes below 2 nm, explaining their absence in previous experiments. Both ⟨100⟩ and ⟨111⟩ loops can result from this transformation, revealing a new mechanism for ⟨100⟩ loop formation that does not require any special constraints. This work significantly advances our understanding in this area and has been summarized into a journal article [67] currently under review.

The relative stabilities between C15 clusters and loops can be elucidated by their formation energies. In our calculations, the size of these clusters varies from a few to over a hundred SIAs to bridge the resolution gap between previous simulations and experiments. To be consistent with the previous study [68], we use the interatomic potential for bcc Fe denoted as M07 [69]. This potential has been shown to give good descriptions of SIA clusters [69], particularly the relative formation energies between C15 clusters and ⟨111⟩ loops in reference to DFT calculations [68]. As shown in Fig. 29, a clear crossover between the formation energies of C15 clusters and loops can be seen. In agreement with previous DFT calculations [68], at small sizes (starting from 4 SIAs) C15 clusters are found to be energetically more favorable than loops. However, beyond a critical size of about 20-30 SIAs, the relative stabilities are reversed. Between the two types of loops, ⟨111⟩ loops are found to be slightly more stable than ⟨100⟩ ones at 0 K for sizes up to 150 SIAs, consistent with previous studies [69]. We note that the MD results also fit well with elasticity theories, as shown in Fig. 29.

The per-SIA formation energies of C15 clusters are much lower than that for an individual SIA (3.73 eV), suggesting that they are strong sinks to SIAs. Therefore, there should be a strong tendency for them to grow by absorbing mobile SIAs, yet they have not been observed in previous experiments. To investigate their absence in experiments, a number of *growth* simulations are performed. In each simulation, a C15 cluster with 5 SIAs is initially created, and individual SIAs are randomly inserted one at a time at nearby locations. Following each insertion, the system is relaxed for 250 ps at 300 K for the newly inserted SIA to diffuse to the cluster. In all *growth* simulations the C15 clusters grow firstly by absorbing SIAs, as expected; however, they all transform into loops later. Both ⟨100⟩ (with three equivalents: [100], [010] and [001]) and ⟨111⟩ ([111]/2, [$\bar{1}$11]/2, [1$\bar{1}$1]/2 and [11$\bar{1}$]/2) loops are possible products, indicating the stochastic nature of this transformation. Among the total 40 *growth* simulations, 70% (29 out of 40) transform into ⟨100⟩ loops and 30% into ⟨111⟩ loops. Sometimes part of the cluster still remains as C15 phase while the majority of it has transformed into a loop. The critical size for the transformation to occur is also stochastic, varying from 56 to 147 SIAs (or 1.3-1.9 nm in diameter) in these simulations, as shown in Fig. 30.

The fate of C15 clusters demonstrated by the *growth* simulations clearly explains the puzzle of their

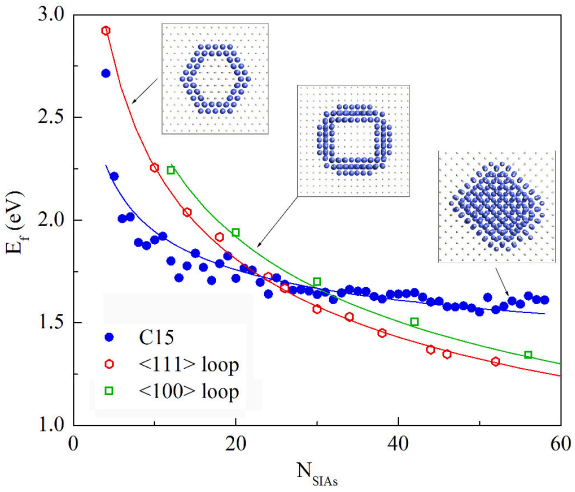

Figure 29: Formation energies per SIA of C15 clusters and prismatic loops at different sizes. From left to right, the insets show the configurations for a ⟨111⟩ loop, a ⟨100⟩ loop and a C15 cluster used in the calculations. bcc Fe atoms are shown as gray dots and non-bcc ones as blue spheres. The solid lines are fitted to elasticity theory.

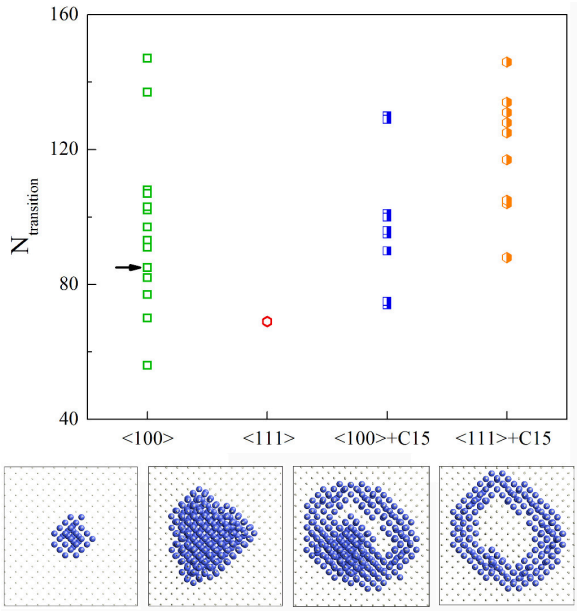

Figure 30: (Top) Statistics for the transitions from C15 clusters to loops obtained by growth simulations. (Bottom) Growth of a C15 cluster and subsequent transition into a ⟨100⟩ loop. From left to right, the cluster contains 6, 54, 85 and 87 SIAs. bcc Fe atoms are shown as gray dots and non-bcc ones as blue spheres.

existence. At sizes beyond the crossover size, the high strain and excess cohesive energies tend to drive the clusters to transform into prismatic loops. The driving force increases as they grow larger in size. Consequently, all C15 clusters eventually transform into loops at sizes too small to be observed by previous experiments.

More importantly, the *growth* simulations reveal a new possible mechanism for ⟨100⟩ loop formation - by transformation from C15 clusters. To further explore the transformation mechanism, a series of *annealing*

simulations are conducted. In each simulation, a C15 cluster is coherently inserted into a bcc matrix, followed by 0.5 ns relaxation at temperatures varying from 600 K to 1200 K. Four initial cluster sizes are used: 26, 58, 95 and 157 SIAs. Transformations into loops are observed for all clusters except for the one with 26 SIAs, due to the comparable energy levels between C15 clusters and loops at that size (see Fig. 29). As the driving force increases with increasing size, transformation towards loops become easier and can be observed at lower temperatures. For the C15 cluster with 157 SIAs, the transformation completes within 0.5 ns at 600 K, while for the one with 58 SIAs, transformations are only observed at 1200K. We note that the temperature-dependent relative stabilities between $\langle 100 \rangle$ and $\langle 111 \rangle$ loops as shown in Dudarev et al. [70] are not established, and no temperature dependence has been seen in the choice of transformation results.

Like in the *growth* simulations, formations of both $\langle 100 \rangle$ and $\langle 111 \rangle$ loops are observed during *annealing*. Similarly, It has been shown that the interaction of two $\langle 111 \rangle$ loops can result in either a $\langle 100 \rangle$ or a $\langle 111 \rangle$ loop [64]. Despite the stochastic nature of the transformation, some common features can still be extracted. As examples, two transformation processes are shown in Fig. 31, with the final products being a [010] and a $[\bar{1}11]/2$ loop, respectively. Here we use the dislocation-extraction-algorithm (DXA) [71] to identify the loop structures and Burgers vectors, with the corresponding atomic configurations shown as insets. Starting from a C15 cluster with 95 SIAs, the transformation begins with the nucleation of $\langle 111 \rangle$ type segments. Multiple $\langle 111 \rangle$ segments may nucleate and evolve into complex loop configurations containing both $\langle 111 \rangle$ and $\langle 100 \rangle$ components. These segments further react with each other to reduce the total loop length and thus energy, until a single loop forms.

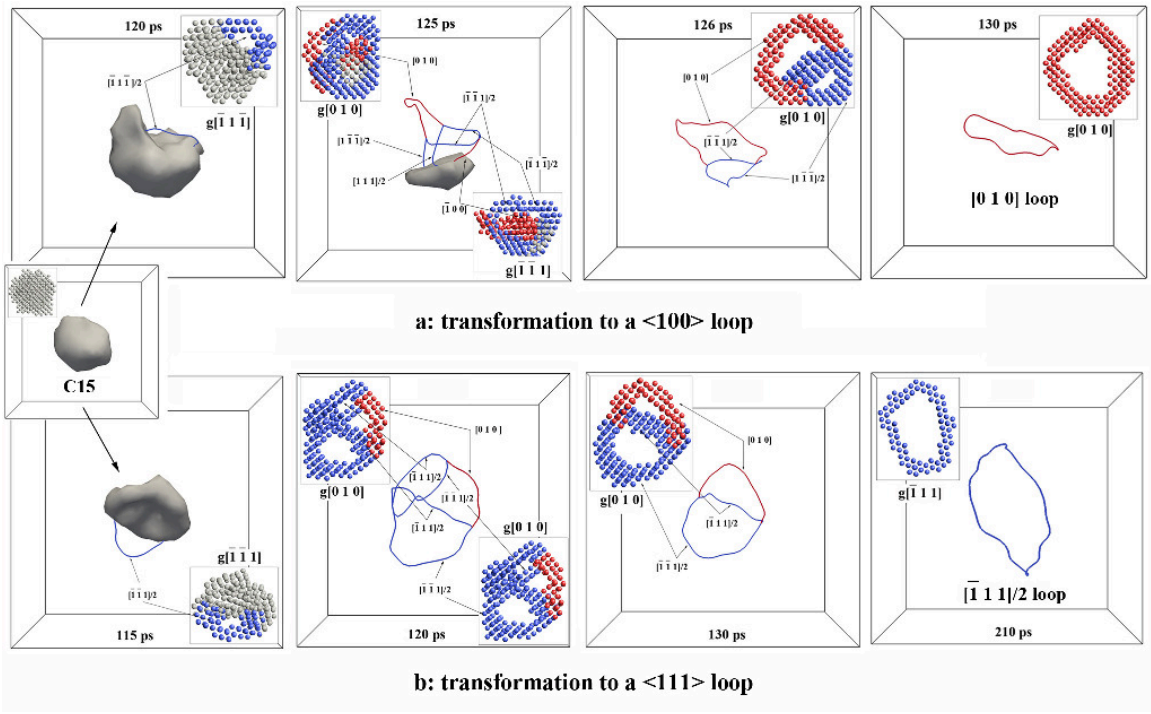

Figure 31: Transformation paths from a C15 cluster (95 SIAs) to a (a) [010] loop and (b) $[\bar{1}11]/2$ loop at 900 K. Insets are the corresponding atomic configurations projected into the plane denoted by the **g** vector. Only non-bcc atoms are shown, with those associated with $\langle 100 \rangle$ segments ($\langle 111 \rangle$) colored in red (blue), and others in gray.

The nucleation of $\langle 111 \rangle$ segments is stochastic in nature and the Burgers vector may take any of the four equivalents. Following nucleation, the subsequent interactions are found to follow the Kirchhoff′s law for dislocation reaction [72], in contrast to the stochastic SIA rearrangement reported previously [64]. As shown

Fig. 31(a), the transformation to a [010] loop starts with the nucleation of a $[\bar{1}1\bar{1}]/2$ segment at 120 ps. At 125 ps, a loop complex forms with 6 segments, including two $\langle 100 \rangle$ ones. The [010] segment is the product of the below reactions:

$$[\bar{1}1\bar{1}]/2 + [111]/2 = [010] \tag{15}$$

$$[\bar{1}\bar{1}1]/2 + [1\bar{1}\bar{1}]/2 = -[010] \tag{16}$$

And the $[\bar{1}00]$ segment forms by:

$$[\bar{1}1\bar{1}]/2 + [\bar{1}\bar{1}1]/2 = [\bar{1}00] \tag{17}$$

The negative sign in the right side of Eq. 16 comes from the different line vectors of the segments involved. At 126 ps, the $[\bar{1}00]$ segments vanishes via the reverse of reaction 17, and the [111]/2 and $[\bar{1}1\bar{1}]/2$ segments react into [010] segment by reaction 15. The two $\langle 111 \rangle$ segments remained at 126 ps continue to react via reaction 16 and eventually, a single [010] loop forms at 130 ps. A similar reaction path can be identified for the path in Fig. 31 (b). Although a [010] segment is seen in the intermediate stage, the final product is a single $[\bar{1}11]/2$ loop. Formation of $\langle 100 \rangle$ segments has been seen experimentally during the absorption of one $\langle 111 \rangle$ loop by another [73], and it does not guarantee the final formation of a single $\langle 100 \rangle$ loop [64].

In addition to the M07 potential, the above presented results have been reproduced by the Mendelev (M03) [74] and the Ackland (A04) [75] potentials, to clarify the dependence of the current results on the interatomic potential. By bridging the gap between previous DFT prediction (sub-nanometer) [68] and experimental observations (beyond a few nm) [66, 76, 73], this work resolves the discrepancy on the existence of C15 phase SIA clusters. These 3D clusters have important impact on long-term defect evolution in bcc steels owing to their superior stability at small sizes and transformation into prismatic loops at large sizes. The transformation mechanisms suggest that $\langle 100 \rangle$ loops may form by clustering of SIAs, with C15 clusters being the intermediate stages. This process does not require pre-existing $\langle 111 \rangle$ loops, which are necessary in all previous proposed mechanisms [63, 64, 77]. Consistently, recent experiments showed that under ion-irradiation $\langle 100 \rangle$ loops form exclusively without presence of $\langle 111 \rangle$ loops at temperatures above 500°C [66]. In the experiments, a special sample orientation has been used to avoid the escaping of $\langle 111 \rangle$ loops at free surfaces, so that their absence indicates that they do not form. Therefore, the present results may provide a better explanation to the experiments. Direct experimental validation of the above results may also be possible, *e.g.*, using high-resolution Transmission-Electron-Microscopy [78].

4.6 Summary and future plan

In summary, in FY 2014 progress has been made at lower length scales under the Grizzly project in the following areas: (1) further development of the AKMC model to convert the KMC time to realistic time by considering the equilibrium thermal vacancy concentration and solute trapping effect; (2) benchmarking of the AKMC simulation with thermal aging experiments on Fe-Cu1.34% mode alloy at 773K; (3) implementation of a nucleation model which is currently demonstrated using the MARMOT application; (4) fundamental understanding on the formation mechanism of$\langle 100 \rangle$ SIA loops and the stability of C15 clusters.

In FY 2015, the focus at the lower length scale will be on development of phase field models for solute precipitation in model RPV alloys including Fe-Cu, Fe-Cu-Ni and Fe-Cu-Ni-Mn, and meso-scale modeling of irradiation damage accumulation. Atomistic simulations will be used to assist these efforts. For solute precipitation, existing free energy functionals will be implemented and tested. The nucleation behavior of solute precipitates will be investigated by coupling phase field and AKMC simulations. For radiation damage, previous approaches in literature will be evaluated, and the most relevant one will be implemented. Some minor effort will also be paid to close out the work reported here, such as finalizing AKMC code development, and preparing this work for presentation in journals and at conferences.

5 References

1. M.K. Samal, J.K. Chakravartty, M. Seidenfuss, and E. Roos. Evaluation of fracture toughness and its scatter in the dbtt region of different types of pressure vessel steels. *Engineering Failure Analysis*, 18:172–185, 2011.

2. S. J. Zinkle and G. S. Was. *Acta Mater.*, 61:735, 2013.

3. J T Busby. Light water reactor sustainability program: Materials aging and degradation pathway technical program plan. , Oal Ridge National Laboratory, 2013.

4. P. L. Andresen, F. P. Ford, F. Gott, R. L. Jones, P. M. Scott, T. Shoji, R. W. Staehle, and R. L. tapping. Nureg/cr-6923: Expert panel report on proactive materials degradation assessment. , U.S. Nuclear Regulatory Commission, 2006.

5. T. Lian. EPRI materials degradation matrix, revision 3. , Electric Power Research Institute, 2013.

6. B Spencer, Y F Zhang, P Chakraborty, S B Biner, M Backman, B Wirth, S Novascone, and J Hales. Light water reactor sustainability program: Grizzly year-end progress report. , Idaho National Laboratory, 2013.

7. D. Gaston, C. Newman, G. Hansen, and D. Lebrun-Grandie. *Nucl. Eng. Des.*, 239:1768, 2009.

8. Benjamin Spencer and Hai Huang. Survey of models for concrete degradation. INL/EXT-14-32925, Idaho National Laboratory, Idaho Falls, ID, August 2014.

9. G R Odette and G E Lucas. *JOM*, 53:18, 2001.

10. G R Odette and R K Nanstad. *JOM*, 61:17, 2009.

11. Benjamin Spencer, Jeremy Busby, Richard Martineau, and Brian Wirth. A proof of concept: Grizzly, the lwrs program materials aging and degradation pathway main simulation tool. , Idaho National Laboratory, 2012.

12. E. D. Eason, G.R. Odette, R.K. Nanstad, and T. Yamamoto. *J. Nucl. Mater*, 433:240, 2013.

13. T. L. Dickson, P. T. Williams, and S. Yin. *Fracture Analysis of Vessels - Oak Ridge FAVOR, v09.1, Computer Code: User's Guide*. Oak Ridge National Laboratory, December 2009.

14. F. Soisson, C.S. Becquart, N. Castin, C. Domain, L. Malerba, and E. Vincent. *J. Nucl. Mater.*, 406:55, 2010.

15. Benjamin Spencer, Marie Backman, Pritam Chakraborty, and William Hoffman. 3d j-integral capability in grizzly. INL/EXT-14-33257, Idaho National Laboratory, Idaho Falls, ID, September 2014.

16. E.D. Eason, G.R. Odette, R.K. Nanstad, and T. Yamamoto. A physically-based correlation of irradiation-induced transition temperature shifts for RPV steels. *Journal of Nuclear Materials*, 433(1-3):240–254, February 2013.

17. K. Wallin. The scatter in K_{IC} results. *Engineering Fracture Mechanics*, 19(6):1085–1093, 1984.

18. ASTM. *Standard Test Method for Determination of Reference Temperature, To, for Ferritic Steels in Transition Range*, 13 edition, 2013.

19. Matthew C. Walters, Glaucio H. Paulino, and Robert H. Dodds. Interaction integral procedures for 3-D curved cracks including surface tractions. *Engineering Fracture Mechanics*, 72(11):1635–1663, July 2005.

20. I.S. Raju and J.C. Newman. Stress-intensity factors for a wide range of semi-elliptical surface cracks in finite-thickness plates. *Engineering Fracture Mechanics*, 11(4):817–829, January 1979.

21. B. Tanguy, J. Besson, R. Piques, and A. Pineau. Ductile to brittle transition of an A508 steel characterized by Charpy impact test. Part II: modeling of the Charpy transition curve. *Engineering Fracture Mechanics*, 72:413–434, 2005.

22. M. K. Samal, M. Seidenfuss, E. Roos, B. K. Dutta, and H. S. Kushwaha. Experimental and numerical investigation of ductile-to-brittle transition in a pressure vessel steel. *Material Science and Engineering A*, 496:25–35, 2008.

23. G. Rousselier. Ductile fracture models and their potential in local approach of fracture. *Nuclear Engineering and Design*, 105:97–111, 1987.

24. A. L. Gurson. Continuum theory of ductile rupture by void nucleation and growth: Part I-yield criteria and flow rules for porous ductile media. *Journal of Engineering Materials*, 99:2–15, 1997.

25. W. Weibull. A statistical distribution function of wide applicability. *Journal of Applied Mechanics*, 18:293–297, 1953.

26. D. A. Curry and J. F. Knott. Effect of microstructure on cleavage fracture toughness in mild steel. *Metal Science*, 13:341–345, 1979.

27. F.M. Beremin. A local criterion for cleavage fracture of a nuclear pressure vessel steel. *Metals and Materials Transaction A*, 14A:2277–2287, 1983.

28. B. Z. Margolin, V. A. Shvetsova, A. G. Gulenko, and V. I. Kostylev. Application of a new cleavage fracture criterion for fracture toughness prediction for RPV steels. *Fatigue and Fracture in Engineering Materials and Structures*, pages 697–713, 2006.

29. P. Chakraborty and S. Bulent Biner. A unified cohesive zone approach to model the ductile to brittle transition of fracture toughness in reactor pressure vessel steels. *Engineering Fracture Mechanics*, 2014.

30. J.A. Joyce and R.L. Tregoning. Determination of constraint limits for cleavage initiated toughness data. *Engineering Fracture Mechanics*, 72(1559-1579), 2005.

31. K. Wallin, T. Planman, M. Valo, and R. Rintama. Applicability of miniature size bend specimens to determine the master curve reference temperature T_0. *Engineering Fracture Mechanics*, 68:1265–1296, 2001.

32. G.R. Odette, T. Yamamoto, H. Kishimoto, M. Sokolov, P. Spatig, W.J. Yang, J.W. Rensman, and G.E. Lucas. A master curve analysis of F82H using statistical and constraint loss size adjustments of small specimen data. *Journal of Nuclear Materials*, 329-333:1243–1247, 2004.

33. M. Nevalainen and R.H. Dodds. Numerical investigation of 3-d constraint effects on brittle fracture in SE(B) and C(T) specimens. , U.S. Nuclear Regulatory Commission, 1995.

34. C. Ruggieri and R.H. Dodds. A transferability model for brittle fracture including constraint and ductile tearing effects: A probabilistic approach. , U.S. Nuclear Regulatory Commission, 1996.

35. J.P. Petti and R.H. Dodds. Coupling of the Weibull stress model and macroscale models to predict cleavage fracture. *Engineering Fracture Mechanics*, 71:2079–2103, 2004.

36. V. Tvergaard. Influence of voids on shear band instabilities under plane strain conditions. *International Journal of Fracture*, 17(4):389–407, 1981.

37. V. Tvergaard and A. Needleman. Analysis of the cup-cone fracture in a round tensile bar. *Acta Metallurgica*, 32(1):157–169, 1984.

38. G.R. Odette and G.E. Lucas. *Irradiation embrittlement of reactor pressure vessel steels: Mechanisms, models and data corrleations*, volume 2, pages 206–241. American Society for Testing and Materials, 1986.

39. A. Arsenlis, M. Rhee, G. Hommes, R. Cook, and J. Martin. A dislocation dynamics study of the transition from homogeneous to heterogeneous deformation in irradiated body-centered cubic iron. *Acta Materialia*, 60:3748–3757, 2012.

40. B. Tanguy, C. Bouchet, S. Buget, and J. Besson. Local approach to fracture based prediction of the ΔT_{56J} and $\Delta T_{KIC,100}$ shifts due to irradiation for an a508 pressure vessel steel. *Engineering Fracture Mechanics*, 73(191-206), 2006.

41. B. Z. Margolin and V. I. Kostylev. Radiation embrittlement modeling for reactor pressure vessel steels: II. Ductile fracture toughness prediction. *International Journal of Pressure Vessels and Piping*, 76:731–740, 1999.

42. B. Gurovich, E. Kuleshova, Y. Shtrombakh, O. Zabusov, and E. Krasikov. Intergranular and intragranular phosphorus segregation in russian pressure vessel steels due to neutron irradiation. *Journal of Nuclear Materials*, 279:259–272, 2000.

43. E. Kuleshova, B. Gurovich, Y. Shtrombakh, D. Erak, and O. Lavrenchuk. Comparison of microstructural features of radiation embrittlement of VVER-440 and VVER-1000 reactor pressure vessel steels. *Journal of Nuclear Materials*, 300(127-140), 2002.

44. C. F. Shih, B. Moran, and T. Nakamura. Energy release rate along a three-dimensional crack front in a thermally stressed body. *International Journal of Fracture*, 30:79–102, 1986.

45. ASTM. *Standard Test Method for Measurement of Fracture Toughness*, 13 edition, 2013.

46. T.L. Anderson. *Fracture Mechanics: Fundamentals and Applications*. CRC Press, New York, USA, 1995.

47. M. Matijasevic, E. Lucon, and A. Almazouzi. Behavior of ferritic/martensitic steels after n-irradiation at 200 and 300 ^{o}C. *Journal of Nuclear Materials*, 377:101–108, 2008.

48. G. R. Odette, M. Y. He, E. G. Donahue, P. Spatig, and T. Yamamoto. Modeling the multiscale mechanics of flow localization-ductility loss in irradiation damaged bcc alloys. *Journal of Nuclear Materials*, 307-311:171–178, 2002.

49. K. Farrell, T. S. Byun, and N. Hashimoto. Deformation mode maps for tensile deformation of neutron-irradiated structural alloys. *Journal of Nuclear Materials*, 335:471–486, 2004.

50. Dassault Systems Simulia Corp., Providence, RI, USA. *ABAQUS version 6.12*, 2012.

51. P. Fernandez, A.M. Lancha, J. Lapena, and M. Hernandez-Mayoral. Metallurgical characterization of the reduced activation ferritic/martensitic steel EUROFER'97 on as-received condition. *Fusion Engineering Design*, 58-59:787–792, 2001.

52. M. Brumovsky, L. M. Davies, A. Kryukov, V. N. Lyssakov, and R. K. Nanstad. *Reference manual on the IAEA JRQ correlation monitor steel for irradiation damage studies*. IAEA, Vienna, Austria, 2001.

53. S. Plimpton, C. Battaile, M. Chandross, L. Holm, A. Thompson, V. Tikare, G. Wagner, E. Webb, X. Zhou, and C. Garcia Cardona. Sand2009-6226: Crossing the mesoscale no-man's land via parallel kinetic monte carlo. , Sandia National Laboratory, 2009.

54. E. Vincent, C.S. Becquart, and C. Domain. Microstructural evolution under high flux irradiation of dilute feâĂŞcunimnsi alloys studied by an atomic kinetic monte carlo model accounting for both vacancies and self interstitials. *J. Nucl. Mater.*, 382:154–159, 2008.

55. Yong Feng Zhang, Paul C. Millett, Michael R. Tonks, Xian Ming Bai, and S. Bulent Biner. Preferential Cu precipitation at extended defects in bcc Fu: An atomistic study. Under review, 2014.

56. F. Soisson and C C Fu. *Phys. Rev. B*, 76:214102, 2007.

57. Laszlo Granasy, Tamas Borzsonyi, and Tamas Pusztai. Nucleation and bulk crystallization in binary phase field theory. *Phys. Rev. Lett.*, 88:206105, 2002.

58. J. P. Simmons, Youhai Wen, C. Shen, and Y. Z. Wang. Microstructural development involving nucleation and growth phenomena simulated with the phase field method. *Materials Science and Engineering: A, Multiscale Materials Modelling*, 365(136âĂŞ143), 2003.

59. M.R. Tonks, D. Gaston, P.C. Millett, D. Andrs, and P. Talbot. An object-oriented finite element framework for multiphysics phase field simulations. *Comp. Mat. Sci.*, 51(1):20–29, 2012.

60. A. N. Stroh. *Phil Mag.*, 3:625, 1958.

61. B. C. Masters. *Philos. Mag.*, 11:881, 1965.

62. B. L. Eyre and R. Bullough. *Philos. Mag.*, 12:31, 1965.

63. J. Marian, B. D. Wirth, and J. M. Perlado. *Phys. Rev. Lett.*, 88:255507, 2002.

64. H. X. Xu, R. E. Stoller, Y. N. Osetsky, and D. Terentyev. *Phys. Rev. Lett.*, 110:265503, 2013.

65. K. Arakawa, M. Hatanaka, E. Kuramoto, K. Ono, and H. Mori. *Phys. Rev. Lett.*, 96:125506, 2006.

66. Z. Yao, M. L. Jenkins, M. Hernandez-Mayoral, and M. A. Kirk. *Philos. Mag.*, 90:4623, 2010.

67. Yong Feng Zhang, Xian-Ming Bai, Michael R. Tonks, and S Bulent Biner. Formation of prismatic loops from c15 laves phase interstitial clusters in body-centered-cubic iron. Under review, 2014.

68. M. C. Marinica, F. Willaime, and J. P. Crocombette. *Phys. Rev. Lett.*, 108:025501, 2012.

69. L. Malerba et al. *J. Nucl. Mater.*, 406:19, 2010.

70. S. L. Dudarev, R. Bullough, and P. M. Derlet. *Phys. Rev. Lett.*, 100:135503, 2008.

71. A. Stukowski, V. V. Bulatov, and A. Arsenlis. *Modelling Simul. Mater. Sci. Eng.*, 20:085007, 2012.

72. J P Hirth and J Lothe. *Theory of Dislocations*. McGraw-Hill, New York, 1968.

73. K. Arakawa, T. Amino, and H. Mori. *Acta Mater.*, 59:141, 2011.

74. M. I. Mendelev, S. Han, D. J. Srolovitz, G. J. Ackland, D. Y. Sun, and M. Asta. *Philos. Mag.*, 83:3977, 2003.

75. G. J. Ackland, M. I. Mendelev, D. J. Srolovitz, S. Han, and A.V. Barashev. *J. Phys. Condens. Matter*, 16:S2629, 2004.

76. B. Yao, D. J. Edwards, and R. J. Kurtz. *J. Nucl. Mater.*, 434:402, 2013.

77. K. Arakawa, K. Ono, M. Isshiki, K. Mimura, M. Uchikoshi, and H. Mori. *Science*, 318:956, 2007.

78. W. Z. Xu, Y. F. Zhang, G. M. Cheng, W. W. Jian, P. C. Millett, C. C. Koch, S. N. Mathaudhu, and Y. T. Zhu. *Nature Communications*, 4:2288, 2013.